2020

High-fidelity Mini-LED and Micro-LED Displays

Yuge Huang
University of Central Florida

HIGH-FIDELITY MINI-LED AND MICRO-LED DISPLAYS

by

YUGE HUANG
B.S. Nanjing University, 2015

A dissertation submitted in partial fulfillment of the requirements
for the degree of Doctor of Philosophy
in the College of Optics and Photonics
at the University of Central Florida
Orlando, Florida

Spring Term
2020

Major Professor: Shin-Tson Wu

ABSTRACT

Mini-LED and micro-LED are emerging disruptive display technologies, because they can work as local dimmable backlight to significantly enhance the dynamic range of conventional LCDs, or as sunlight readable emissive displays. However, there are still unresolved issues impairing their display fidelity: 1) motion blur on high-resolution, large-size and high-luminance devices, 2) limited contrast ratio on mini-LED backlit LCD (mLED-LCD), 3) relatively high power consumption, and 4) compromised ambient contrast ratio. This dissertation tackles with each of these issues for achieving high display fidelity.

Motion blur is caused by slow liquid crystal response time and image update delays. Low-duty ratio operation can suppress motion blur in emissive displays. However, it induces driving burdens on high-resolution, large-size and high-luminance mLED-LCD panel electronics and demands fast-response liquid crystals. In order to overcome these challenges, in Chapter 2, we propose a novel image-corrected segmented progressive emission method for mitigating the motion blur of mLED-LCDs. In parallel, in Chapter 3 and Chapter 4, we report new liquid crystal materials with submillisecond response time.

High dynamic range displays require high peak luminance, true black state and high contrast ratio. While emissive displays intrinsically exhibit high contrast ratio, for LCDs it is limited to 1000:1 ~ 5000:1. In Chapter 5, we develop a simplified model for optimizing mLED-LCD to suppress the halo effect and achieve the same image quality as emissive displays. On the other hand, high luminance may give rise to short battery time and thermal management issues in displays with low power efficiency. In Chapter 6, we build a new model for mini-LED/micro-LED displays to simulate and optimize the power efficiency. In Chapter 7, we jointly consider the LED

external quantum efficiency, system optical efficiency and structure-determined ambient light reflection to guide the designs for high ambient contrast ratio with optimal efficiency.

For a better world.

ACKNOWLEDGMENTS

I received so much love and so many supports during my Ph.D. years. That experience is precious and memorable. Without them, I will never make so many achievements.

I would give my earnest appreciation to my thesis adviser, Dr. Shin-Tson Wu. He is visionary, persistent, always patient and kind. He created many opportunities to provide trainings and inspirations. He encouraged me to see things from a wider scope and to do better and better. On him I see God's blessings and an unreserved educator. And I would express my thankfulness to Cho-Yan Hsieh, Dr. Wu's better half. She made a warm home for us international students, taking good care of us with considerate and consistent love.

I would give my sincere gratitude to my committee members: Dr. M. G. Moharam, Dr. Patrick L. LiKamWa and Dr. Yajie Dong. They are knowledgeable and respectable scientists, loving students and supportive. I feel so grateful for having them in my Ph.D. years. They are making a better CREOL.

I would like to thank my groupmates. Senior students Dr. Daming Xu, Dr. Fenglin Peng, Dr. Ruidong Zhu, Dr. Haiwei Chen, Dr. Yun-Han Lee, Dr. Hao Chen and Dr. Guanjun Tan set up great role models. They were always nice and patient when clearing up my confusions, teaching me simulations and instructing me on experiments. Dr. Juan He, Fangwang Gou, Caicai Zhang and Kun Yin are lovely ladies. They made the atmosphere diversified and active. Junior students Ziqian He, Tao Zhan, Jianghao Xiong, Yannanqi Li, En-Lin Hsiang, Junyu Zou, Qian Yang and Zhiyong Yang are talented. Wish they unleash their potentials and contribute to the society. I would thank Dr. Md Javed Rouf Talukder, Dr. Ran Chen, Ming-Yang Deng, Dr. Enguo Chen, Dr. Sang-Hun Choi and Guigeng Liu. I had great collaborations with them.

I would express my thankfulness to my research collaborators. Dr. Jiun-Haw Lee was always patient answering my OLED questions and is generous in uplifting young students. I hope to be a professional like him. Dr. Eiji Okabe from JNC Corp. and Kifumi Yoshidaya from DIC Corp. were very kind and responsive in our collaborations on LC materials. Engle Liao is experienced in LCoS R&D and helped me on every of my questions. Jhou-Pu Yang and I have complementary skills and he taught me a lot.

I would like to thank Dr. Lu Lu, Dr. Junren Wang, Dr. Yusufu Sulai, Dr. Yang Zhao, Dr. Weichuan Gao, Dr. Ying Geng, Dr. Jacques Gollier and Dr. Barry Silverstein from Facebook Reality Labs. And I would like to thank Dr. Yanqing Lu, Dr. Wei Hu, Dr. Xiaoyong Wang, Dr. Renbiao Wu, Dr. Zhaojun Liu, Dr. Huai Yang, Dr. Qionghua Wang, Dr. Zhongwei An, Min Yu, Dr. Qun Yan, Dr. Hongxia Zhang, Dr. Ling Wang, Dr. Haitao Dai, Dr. Hongbo Lu, Dr. Yan Li and Dr. Yun-Hsing Fan. They offered me valuable suggestions and supports, opened my eyes and revealed a larger world. I appreciate it.

I would like to thank Dr. Fan Wu, Steffen Wittek, Sepehr Benis and Latifah Maasarani for the time in CREOL Association of Optics Students. I admire their leadership and am influenced by them. I would like to thank Dr. Kyle Renshaw, Zheyuan Zhu, Chenyi Zhang, Lawrence Trask and Suyuan Chen. We established so many “firsts” in IEEE Photonics Society Orlando Section/UCF Student Chapter. They are reliable and passionate teammates.

I would like to thank Zhean Shen, Jianxiong Zhu, Wei Yan, Yuman Fang, Huizhong Ren, Xiaowen Hu, Ruitao Wu, Dr. Guifang Li, Dr. Jianhua Liu, Yingji Gao, Paula Disbrow, Daniel Disbrow, Michel Machado, Fei Jia, Dr. Qitian Ru, Dr. Yangyang Sun, Dr. Jialei Tang, Rachel Franzetta, Peggy Grip, Tom Swartz, Dr. Sheng-Pin Lin and Rowel Go. They took good care of me, making Orlando wonderful. And I would like to thank my dear families. They gave me love and courage to conquer this long journey.

Thank you all.

TABLE OF CONTENTS

LIST OF FIGURES

LIST OF TABLES

CHAPTER 1 INTRODUCTION

Over the past century, display technology has been advanced tremendously. In 1920s, bulky and heavy cathode ray tube (CRT) display opened the display market. Since 2000s, high-image-quality and high-reliability non-emissive liquid crystal display (LCD) became the mainstream [1-6]. Later, new features such as thinner and flexible profile are desirable. In the past decade, emissive organic light-emitting diode (OLED) display has grown rapidly and stands out especially in mobile devices and TVs for the advantages of lesser thickness, free form factor and exceptional dark state [7-13]. However, some critical issues such as burn-in and lifetime remain to be improved [14-16]. Recently, the emerging micro-LED (μLED) [17-20] and mini-LED (mLED) [19,21] technologies are receiving increasing attention for promising features of fast response time, high dynamic range, low power consumption, long lifetime, free form factor etc. Both μLED and mLED can be used as emissive displays, where each LED chip serves as a subpixel. While mLED can also be two-dimensionally arrayed in the backlight unit of LCD to fulfill local dimming function. Presently, mLED/μLED displays are still immature for mass production due to the challenges in optical performance, manufacturing and cost. This dissertation is dedicated to address technical challenges from the aspect of optical system design and display performance. Specifically, we concentrate on four criteria: motion blur, contrast ratio, power efficiency and ambient contrast ratio. Three system configurations – RGB-chip emissive display, color conversion emissive display and mini-LED backlit LCD (mLED-LCD) – are analyzed.

The first study is in motion blur, which has been presented by motion picture response time [22,23]. Motion blur is the image persistence observed on fast-moving objects in display. As shown in Figure 1-1, when the object in Figure 1-1(a) is moving at a high speed on the screen, viewers may notice a blurry profile as Figure 1-1(b) shows. Image persistence comes from slow pixel response time and image update delays; the former reflects the switching speed of each pixel, and the latter is determined by emission pattern. In mLED/μLED emissive displays, LED response time is negligible so that motion blur can be alleviated by increasing frame rate or by employing low-duty-ratio simultaneous emission pattern. In mLED-LCD, the application of above two methods is limited because of three-folded reasons: 1) High-resolution and large-size panels require relatively long data input time so that high frame rate is not preferred. 2) High duty ratio helps maintain high luminance and prevents LED from working in the low efficiency region. 3) Slow liquid crystal (LC) response time could make the efforts on emission pattern innovation in vain. In order to mitigate motion blur in high-resolution, large-size and high-luminance mLED-LCDs, we propose and verify an image-corrected segmented progressive emission pattern in Chapter 2, and report new submillisecond LC materials in Chapter 3 and Chapter 4.

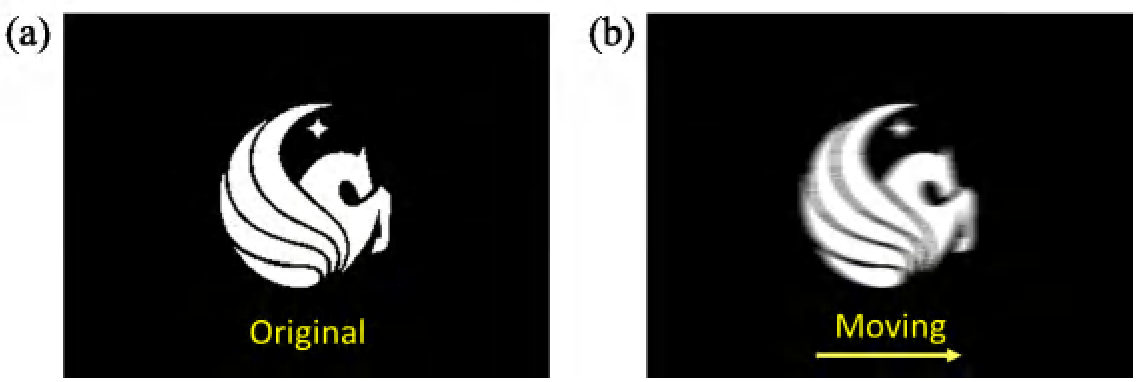

Figure 1-1 Illustration of motion blur. (a) Original profile of the displayed object. (b) Perceived blurry profile when the object is moving with a high speed in display.

High dynamic range displays require high peak luminance, uncompromising black state and high contrast ratio [24-26]. Our second study is in contrast ratio. While emissive displays intrinsically exhibit > 1 000 000:1 contrast ratio, for LCDs it is limited to 1000:1 ~ 5000:1. Mini-

LED backlight unit can enhance LCD's contrast ratio by local dimming [21,27-30]. The backlight is segmented into zone structure; each zone contains several mLED chips to control the panel luminance and each zone can be independently turned-on and -off. However, local dimming LCDs are vulnerable to halo effect. For example, Figure 1-2(a) shows the target image content, but the displayed image on a local dimming LCD can be like Figure 1-2(b). Around the bright object we can see severe light leakage – the so-called halo. Halo effect can be alleviated by increasing the LCD contrast ratio, using larger number of local dimming zones and confining light in each zone. However, these solutions also lead to increased panel cost. In order to know how many local dimming zones and which light profiles are required for faithful image reproduction, in Chapter 5, we develop a model for simulating and optimizing mLED-LCD system. We demonstrate that halo effect and clipping effect can be suppressed to an unnoticeable level on mLED-LCD, and the image quality can be as high as emissive displays.

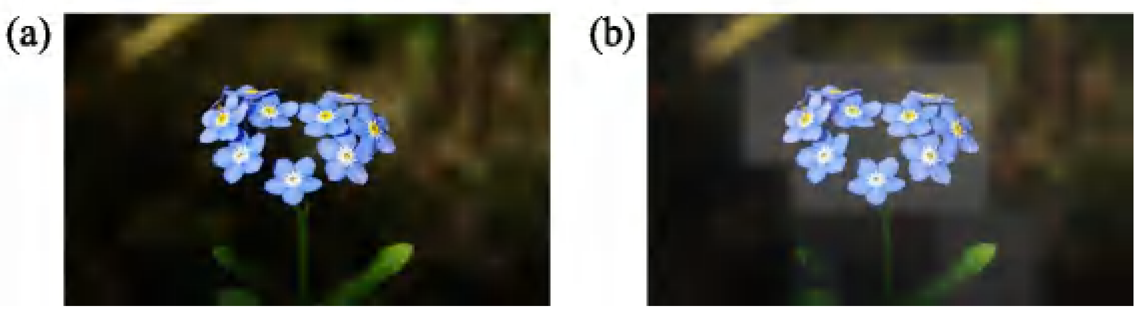

Figure 1-2 (a) Target image. (b) Local dimming displayed image with halo effect around the bright object.

The third study is in power efficiency. High power efficiency is a prerequisite to achieve high luminance in high dynamic range display, which prevents short battery time and thermal management issues. Mini-LED/Micro-μLED emissive displays have high optical efficiency and long lifetime. However, the external quantum efficiency of inorganic mLED/μLED is very sensitive to chip size and current density [20,31,32]. If improperly operated, most of the energy will be consumed by non-radiative recombination and the power efficiency could be pretty low. In order to resolve this issue, in Chapter 6, we build a model considering both LED physics and optical system structures for simulating and optimizing the power efficiency of mLED/μLED displays. The model is found in good agreement with experimental measurements.

Nevertheless, we care about practical application scenarios. Similar to OLED displays, mLED/μLED emissive displays are vulnerable to ambient reflection, which degrades the perceived ambient contrast ratio (ACR) [33]. The focus of our fourth study – ACR is determined by three factors: the ambient illuminance, the display peak luminance and the luminous reflectance of the panel. Increasing display luminance helps enhance ACR, which can be achieved by the methods discussed in Chapter 6. Furthermore, in Chapter 7 we investigate in the luminous reflectance change with optical structures. Considering both power efficiency and luminous reflectance, we define a figure-of-merit to systematically optimize the structure of mLED/μLED emissive displays, and suggest system configurations to provide the highest ACR.

CHAPTER 2 MOTION BLUR SUPPRESSION

2.1 Introduction

Motion blur is the image persistence observed on fast-moving objects in displays. This defect is caused by slow pixel response time and image update delays. The first factor – pixel response time – is material determined. It is at nanosecond level for inorganic LEDs and quantum dot color convertors, at microsecond level for organic LEDs, and takes a few milliseconds in LCDs. To suppress motion blur, submillisecond pixel response time is highly desirable. It has been satisfied on mLED/μLED emissive displays, while remains challenging on mLED-LCD. To resolve this issue, we will report new LC materials with submillisecond response time in Chapter 3 and Chapter 4.

In this chapter, we concentrate on the second factor – image update delays, which is related to emission pattern. Continuous progressive emission is the dominant emission pattern in LCD. Whereas, in order to mitigate motion blur in this emission pattern, panels need to be operated at high frame rate, indicating high power consumption. Simultaneous emission with low duty ratio can effectively suppress motion blur in emissive displays [22,23]. However, the application of simultaneous emission on LCD is mainly constrained in small-size and low-luminance virtual reality panels [34]. On the contrary, large panels normally utilize low-cost a-Si TFTs (amorphous silicon thin-film transistors) and require relatively long data input time, which is the short plate of simultaneous emission. Segmented progressive emission detours the slow LC response time issue of local dimming LCD [35], but suffers from relatively long image update delay. In this chapter, we propose a subframe image content correction method for segmented progressive emission pattern. It works for high-resolution, large-size and high-luminance mLED-LCD. In subjective experiments, we prove that our new method alleviates motion blur significantly.

2.2 Image persistence time

Previously, the analysis of image persistence was mainly focused on temporal delay – presented by motion picture response time (MPRT) [22,23] – while spatial delay also elongates image persistence time (t_{image}). In order to describe image update delay accurately, we consider both temporal delay and spatial delay in continuous progressive emission, simultaneous emission and segmented progressive emission patterns, and use t_{image} as the metric of motion blur.

2.2.1 Continuous progressive emission

Continuous progressive emission is the mainstream choice for the merits of wide compatibility with different display technologies, simple circuitry design and low charging burden. Figure 2-1 illustrates the continuous progressive emission patterns for a conventional active matrix (AM) LCD [Figure 2-1(a)], an AM emissive display [Figure 2-1(b)], and a passive matrix (PM) emissive display [Figure 2-1(c)]. As the axis at the bottom of Figure 2-1 denotes, in horizontal direction is the time axis. Here we plot *Frame k* and *Frame k+1*. In vertical direction is a spatial axis. From the top to the bottom of each schematic are the 1st row to the Nth row. In each frame, the signal is updated row by row via sequentially opening gate transistors $G_1 \sim G_N$. In *Frame k*, the gates are opened along the left hypotenuses of the magenta parallelogram. The corresponding data input time (t_{scan}) equals to frame time (T_f). As an example, the data input time per row of a

60-Hz 4K2K-resolution panel is T_f / N_{gate} = 16.7 ms / 2160 rows = 7.72 μs/row. This relatively long data input time helps accomplish effective charging. The unsynchronized signal update on each row causes spatial delay. This spatial delay can be presented by 0.8 t_{scan}, in which time duration from 10% to 90% spatial area is updated.

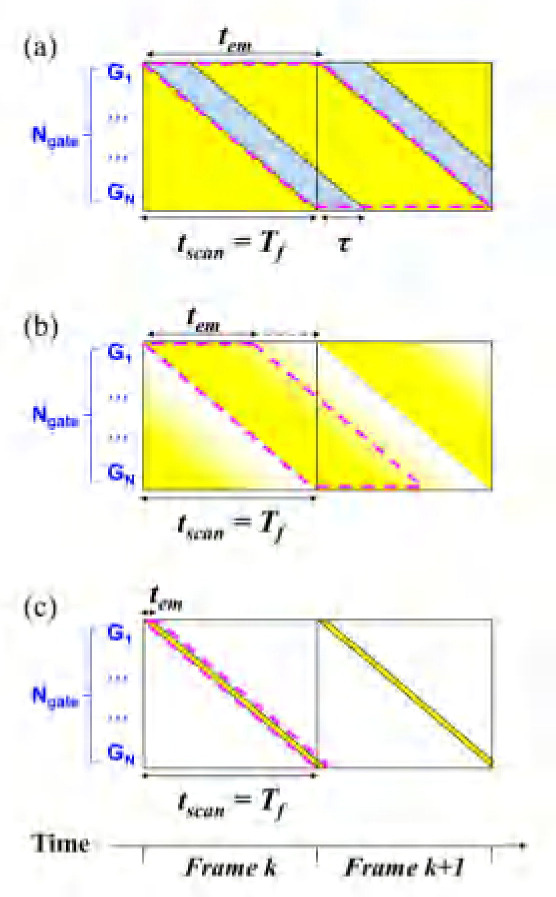

Figure 2-1 Continuous progressive emission patterns of (a) a conventional AM LCD, (b) an AM emissive displays and (c) a PM emissive displays.

For each row, the temporal delay is generated from pixel response time (τ) and LED emission time (t_{em}). In Figure 2-1, τ is the width of the blue parallelograms, which normally takes a few milliseconds in conventional LCDs and is negligible in emissive displays. The yellow color in Figure 2-1 denotes the light emission period. In conventional LCDs [Figure 2-1(a)], the backlight is turned on for the whole frame. In AM emissive displays [Figure 2-1(b)], the t_{em} can be either T_f under pulse amplitude modulation or shorter under pulse width modulation. A combination of driving current control and pulse width control, called hybrid modulation, may also be applied. In PM emissive displays [Figure 2-1(c)], LEDs emit light only when that row is scanned to, resulting in an ultrashort t_{em}. Experientially, Peng et al. proposed a simplified equation to estimate MPRT of conventional LCD with continuous progressive emission pattern [Figure 2-1(a)], which is a good representative of temporal delay [23]:

$$MPRT = \sqrt{\tau^2 + \left(0.8T_f\right)^2}. \tag{2-1}$$

The magenta parallelograms in Figure 2-1 mark the image persistence of *Frame k*. Counting both spatial delay (0.8 t_{scan}) and temporal delay (MPRT), t_{image} of continuous progressive emission pattern is

$$\begin{aligned} t_{image} &= 0.8t_{scan} + MPRT \\ &= 0.8T_f + \sqrt{\tau^2 + \left(0.8t_{em}\right)^2}. \end{aligned} \tag{2-2}$$

Increasing frame rate ($f = 1 / T_f$) can effectively reduce t_{image}. Whereas, the tradeoff is an increment of power consumption, data transmission rate and panel data input time. As a result, the frame rate of high resolution device is limited. For instance, Sony's 98-inch 8K4K-resolution TV (XBR-98Z9G) supports a signal rate of up to 120 Hz at 2K1K resolution, while the maximum rate is 60 Hz at 4K2K resolution and 30 Hz at 8K4K resolution.

2.2.2 Simultaneous emission

Simultaneous emission can dramatically reduce t_{image} at low frame rate. As illustrated in Figure 2-2, the LEDs only emit light when data input process and pixel response are ready. Therefore, spatial delay no longer aggravates image persistence. This emission pattern can be realized by global dimming the LCD backlight or through circuitry adjustment in emissive displays. In order to reserve enough time for data input process and pixel response, t_{em} is short and the duty ratio ($DR = t_{em} / T_f$) is typically $\leq$ 10%. Under such a circumstance, the t_{image} in simultaneous emission is

$$t_{image} = MPRT = 0.8t_{em}. \quad \text{(2-3)}$$

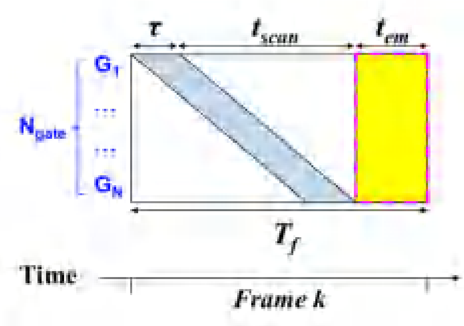

Figure 2-2 Simultaneous emission pattern for LCDs and emissive displays.

Simultaneous emission enables submillisecond t_{image} on emissive displays. For instance, t_{image} = 0.9 ms in a 10%-DR 90-fps display. However, the story is different on high-resolution, large-size and high-luminance mLED-LCD panels. From $t_{scan} + \tau + t_{em} \leq T_f$, the competence between the three time consuming parts is stiff. First, longer data input time (t_{scan}) is required when display resolution increases, especially on large panels where low-cost a-Si TFTs are employed. Second, τ is not an ignorable factor in mLED-LCDs. Third, the required instant luminance is 1 / DR times (e.g. 10 times for DR = 10%) higher than whole-frame-backlight-on displays. Such a high luminance not only demands high current operation, but also shifts the LED working spot to low-efficiency region and exacerbates heat dissipation issues. Consequently, relatively high *DR* is preferred for high luminance. However, either of the two ways for increasing *DR* – increasing t_{em} or decreasing T_f – leads to a decrease of the $t_{scan} + \tau$ budget. Because of the abovementioned reasons, the application of simultaneous emission in LCD is mainly constrained in small-size and low-luminance virtual reality panels [34].

2.2.3 Segmented progressive emission

Segmented progressive emission is designed for local dimming LCDs, but also works for emissive displays. In this emission pattern, the panel is divided into several unit blocks. As an example, Figure 2-3 is an illustration of $N_{block} = 4$ blocks. The data input process and pixel response are the same as continuous progressive emission [Figure 2-1(a)]. The difference is on the time window of LED emission. As shown in Figure 2-3, the blocks are illuminated sequentially. On each block, the backlight is turned on when the data input and pixel response have been finished. So the LC transition no longer impairs image quality. In this design, the constraint of $t_{scan} + \tau + t_{em} \leq T_f$ in simultaneous emission is broken. Instead, $t_{scan} = T_f$ is enabled for high-resolution and large-size panels. And $\tau + t_{em} \leq T_f$ considerably loosens the budget on LC response time and improves *DR* for high-luminance displays. Furthermore, if only one block is illuminated during each time window (as illustrated in Figure 2-3), the number of driver ICs can be reduced to $1 / N_{block}$ of the original amount, indicating a lower IC cost. The corresponding emission time is $t_{em} \leq T_f / N_{block}$, so the instant luminance should be boosted to at least N_{block} times of the original.

The major inadequateness of segmented progressive emission is the slow t_{image}. As the magenta polygon marks in Figure 2-3, spatial delay causes image persistence in segmented progressive emission:

$$t_{image} = 0.8t_{scan} = 0.8T_f. \quad \textbf{(2-4)}$$

For instance, to achieve 2-ms t_{image}, in this emission pattern it needs 400-fps high frame rate operation, facing the same challenge as continuous progressive emission.

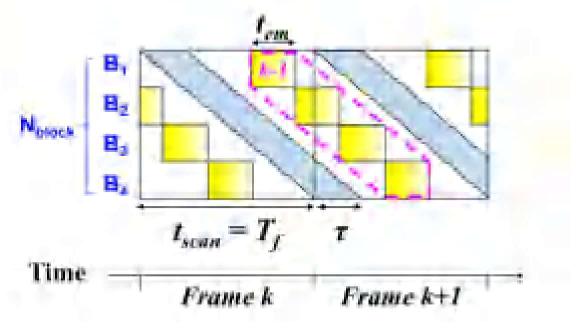

Figure 2-3 Segmented progressive emission pattern without subframe image content correction.

2.3 Subframe image content correction method

2.3.1 Operation principles

In order to significantly reduce t_{image}, we propose a subframe image correction method for segmented progressive emission pattern. In the exemplary illustration in Figure 2-4, four different image contents *k-1*, *k-2*, *k-3* and *k-4* are delivered to the N_{block} = 4 units in *Frame k*. Figure 2-5(a) shows the image content, where the panel is displaying a car moving from the left to the right of the screen. Since blocks #1 to #4 are turned on sequentially, the real car location at each illumination time is changing. In conventional designs with the emission pattern of Figure 2-3, because the content is refreshed once per frame, only image content *k-1* is displayed through the whole panel, as Figure 2-5(b) depicts. The content mismatch between Figure 2-5(a) and Figure 2-5(b) results in motion blur. In our proposed method with the emission pattern of Figure 2-4, the image content at each block is corrected at subframe level, as Figure 2-5(c) illustrates. The persistence of each image content is reduced to

$$t_{image} = 0.8t_{em} = 0.8\frac{t_{scan}}{N_{block}}. \quad \textbf{(2-5)}$$

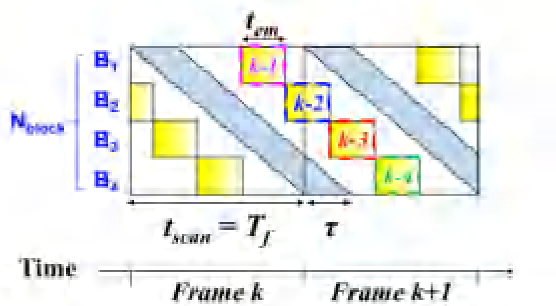

Figure 2-4 Segmented progressive emission pattern with subframe image content correction.

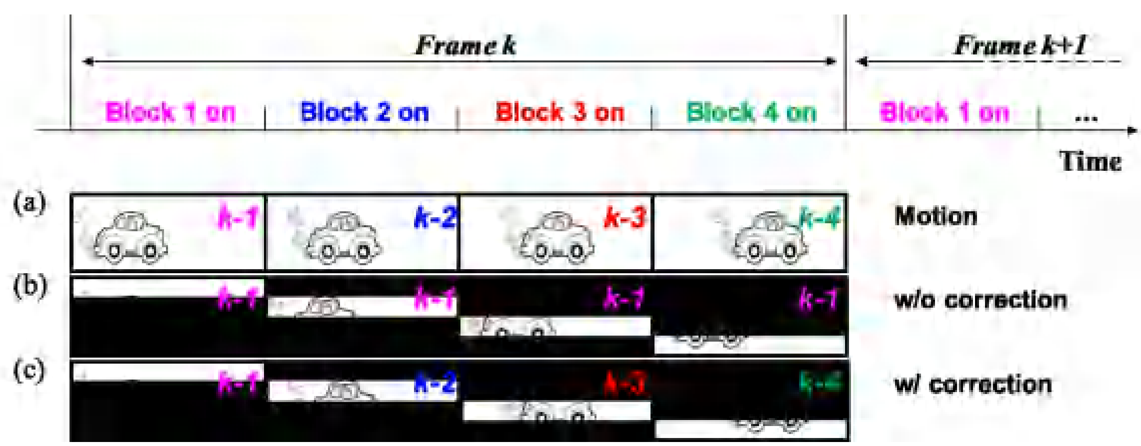

Figure 2-5 Display image content of a car moving from the left to the right of the screen. (a) Real-time car location on screen. (b) Displayed content under segmented progressive emission without subframe image correction. (c) Displayed content under segmented progressive emission with subframe image correction.

2.3.2 Subjective experiment validation

In order to verify the effectiveness of our method, we conducted the following subjective experiments. In a darkroom, we displayed a moving object and a reference static object as shown in Figure 2-6. A DMD (digital micromirror device) projection display with $\tau << T_f$ was employed so that we can focus on the delay from emission pattern and exclude the influence of τ. The projected image has 1024×768 resolution, and was located at a viewing distance for human eye perception limit (60 pixels per degree). The moving speed of the top object was set to be 24° per second angularly. We displayed the video under segmented progressive emission pattern with subframe image content correction and 60-fps frame rate. Ten observers with normal or corrected normal vision were asked to pursuit the moving object and to judge the sharpness difference from the reference static object. Five-point image quality scale was used with half-point score accepted: grades [1~5] represent for [completely different / very different / different / slightly different / identical].

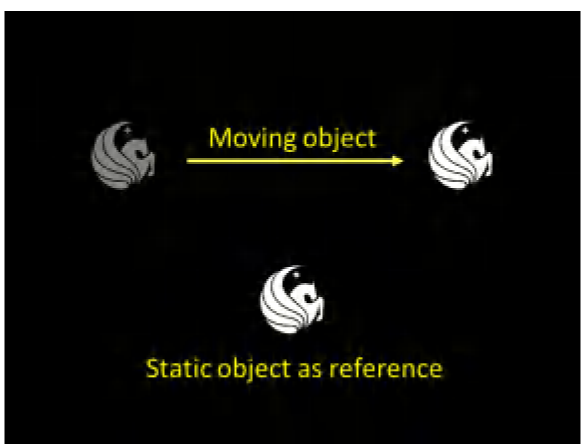

Figure 2-6 Image content used in motion blur evaluation subjective experiment.

The performance of different N_{block} was evaluated and Figure 2-7 shows the average grades. Without image content correction (N_{block} = 1), the average grade is 4: the sharpness of the moving object is slightly different from the static reference. That image quality meets the minimum acceptable level because of the 60-fps frame rate, which has been optimized to and used in display industry for decades. However, advanced displays call for better performance. As shown in Figure 2-7, as N_{block} increases, observers gave higher scores on the perceived image quality, which means motion blur is effectively alleviated. When $N_{block} \geq 3$ (image content rate $\geq$ 180 fps, $t_{image} \leq 4.4$ ms), the perceived image quality grade is higher than 4.5, indicating that more than half of the observers did not notice motion blur. When N_{block} reaches 6 (image content rate $\geq$ 360 fps, $t_{image} \leq 2.2$ ms), the grade is approaching 5: the sharpness of the moving object looks identical to the static reference.

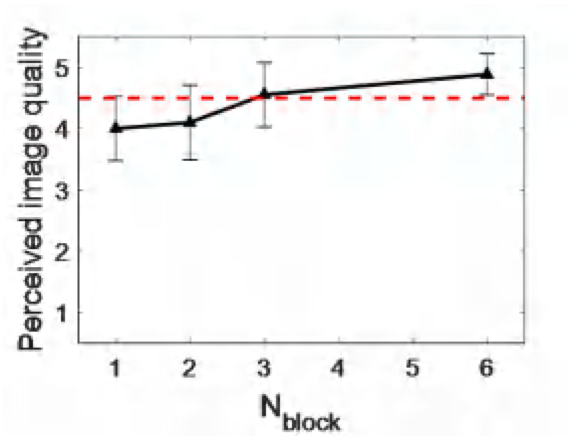

Figure 2-7 Perceived image quality of a 24°/s-moving object in a 60-fps display. The emission pattern is segmented progressive emission and different block numbers in subframe image correction were evaluated.

Image-corrected segmented progressive emission pattern has some requirements. It needs local dimming backlight and higher image content rate than simultaneous emission. From Figure 2-7, at least 180-fps video source is recommended. However, it does not demand such a high data transmission rate on the panel port. The high-frame-rate video source can be processed and compressed to low-frame-rate image content (image recombination from Figure 2-5(c)) before loaded to the display panel so that the data transmission rate on hardware is not necessarily to be increased.

In exchange, this design presents several advantages. Table 2-1 is a comparison of different emission patterns. We can see that image-corrected segmented progressive emission integrates the merits of all other designs. First, it exhibits the shortest image persistence time (= 0.8 t_{em}) as simultaneous emission for motion blur suppression. Second, it provides the longest data input time (= T_f) as continuous progressive emission to release the burdens on electronics, which is especially important to high-resolution and large-size mLED-LCD panels. Third, it enables higher duty ratio than simultaneous emission with the same t_{image}. Numerical examples are given in Table 2-2 to show the improvement from simultaneous emission to image-corrected segmented progressive emission. In Table 2-2, emission pattern #1 and #3 provide the same data input time and image persistence time, while 44% higher duty ratio (indicating higher luminance) can be obtained on pattern #3. Emission pattern #2 and #3 have the same duty ratio and image persistence time, while pattern #3 enables 83% longer data input time for effective signal update. In Table 2-2, we assumed very fast LC response time (τ = 1 ms) in calculation. The improvement from simultaneous emission (#1 and #2) to image-corrected segmented progressive emission (#3) would be bigger if slower LCs are adopted.

Table 2-1 Comparison of the specified emission patterns.

Emission pattern	Continuous progressive	Simultaneous	Segmented progressive	
			Image uncorrected	Image corrected
Emission time	T_f	$T_f - t_{scan} - \tau$	T_f / N_{block}	T_f / N_{block}
Image persistence time	$0.8T_f + \sqrt{\tau^2 + (0.8t_{em})^2}$	$0.8\ t_{em}$	$0.8\ T_f$	$0.8\ t_{em}$
Data input time	T_f	$T_f - t_{em} - \tau$	T_f	T_f
Duty ratio	100%	t_{em} / T_f	t_{em} / T_f	t_{em} / T_f

Table 2-2 Numerical examples of achieving t_{image} = 2.2 ms in the specified emission patterns. Fast LC response time (τ = 1 ms) is assumed in calculation.

Emission pattern	Simultaneous		3-block image-corrected segmented progressive
	#1	#2	#3
Frame rate	83 fps	120 fps	120 fps
Image content rate	83 Hz	120 Hz	360 Hz
Emission time	2.8 ms	2.8 ms	2.8 ms
Data input time	8.3 ms	4.6 ms	8.3 ms
Duty ratio	23%	33%	33%
Image persistence time	2.2 ms	2.2 ms	2.2 ms

2.4 Conclusion

In this chapter, we analyzed the image persistence time in different display patterns considering both temporal delay and spatial delay. A new image-corrected segmented progressive emission method for mLED-LCD was proposed. Our design breaks the tradeoff between image persistence time, data input time and duty ratio in conventional emission patterns. These three parameters determine motion blur, display resolution/panel size and peak luminance, respectively. In subjective experiments, we proved that our method can significantly alleviate motion blur. We recommend at least 180-Hz/preferred 360-Hz image content rate to diminish motion blur. Our new method is designed for mLED-LCD, but also works for emissive displays.

CHAPTER 3 SUBMILLISECOND RESPONSE BLUE PHASE LIQUID CRYSTAL

3.1 Introduction

Fast LC response time is crucial for motion blur mitigation. In this chapter, we report a submillisecond polymer-stabilized blue phase liquid crystal (PS-BPLC) [36,37] material, which has been published in [38]. PS-BPLC is an attractive display technology for the merits of submillisecond response time, no need for surface alignment, optically isotropic dark state, and insensitive to the cell gap in an in-plane switching (IPS) cell [39]. However, it remains at the prototype stage [40,41] because of two major hurdles: 1) high operation voltage (V_p), which leads to high power consumption, and 2) slow capacitor charging in active addressing scheme, which limits the frame rate and resolution of displays. In order to reduce V_p, protruded electrodes [42,43] and large Kerr constant BPLC materials [44-46] have been practiced. Several BPLC materials with $\Delta n > 0.18$ and $\Delta\varepsilon > 100$ have been developed for Kerr constant enhancement [47,48]. However, for such a huge $\Delta\varepsilon$ BPLC material, there are several concerns: 1) increased rotational viscosity (γ_1), which leads to a slower response time (> 1 ms), and 2) longer capacitor charging time when addressed by TFTs (thin film transistors), which is aggravated as frame rate and resolution increase. To overcome the slow charging issue, bootstrapping driving, i.e. pre-charging method has been developed [49,50]. If the average dielectric constant (ε') is smaller than 100, then the charging issue can still be managed. But the dilemma stays: lower $\Delta\varepsilon$ leads to increased V_p. Therefore, a delicate balance between operation voltage, response time, and charging time has to be taken into consideration. An ideal BPLC should possess following properties: fast charging time for high resolution and high frame rate, high transmittance at 15 V for single-TFT driving, and submillisecond response time.

In this chapter, we report a fast-response BPLC mixture, called JC-BP08. Its physical properties are listed as follows: $\varepsilon' \approx 87$ so that the TFT charging issue is still manageable, voltage holding ratio > 99.4% at 25°C once charged, and response time 0.83 ms at room temperature. Using a protruded electrode structure, our simulation results indicate that we can obtain transmittance ~ 74% at 15 V using JC-BP08. This is an important step towards single TFT (per pixel) addressing.

3.2 Material characteristics

In the past few years, three commercial BPLC mixtures have been well studied; they are PSBP-01 (JNC, Japan) [44,48,51], Merck BPLC [47], and HTG-135200 (HCCH, China) [52,53]. Among them, Merck's mixture is only available to some specific customers. JNC's PSBP-01 has a relatively large Kerr constant, which helps to lower the operation voltage. However, its decay time is around 1.6 ms, and is slower at low gray levels. Finally, the HCCH's mixture is for experimental studies only, not intended for active matrix display applications because of its relatively low voltage holding ratio ($VHR \approx 80\%$) [53].

Here, we prepared a new BPLC mixture: JC-BP08 (from JNC). The compositions and UV curing conditions are described as follows: JC-BP08 precursor contains 84 wt. % nematic LC host, 4.8% chiral dopant, 10.8% monomers, and 0.4% photoinitiator. The dielectric anisotropy and birefringence of the LC host of JC-BP08 are $\Delta\varepsilon = 114$ (at frequency 1 kHz and 25°C) and $\Delta n = 0.161$ ($\lambda = 589$ nm and 25°C), respectively. Before UV curing, the phase transition temperatures are: N* 53.0°C BP during heating and BP 50.8°C N* during cooling, where N* stands for chiral nematic phase. After UV curing at BP-I, the physical properties of polymer-stabilized JC-BP08 are: ε' = 87 at frequency f_{AC} = 60 Hz and 25°C, clearing temperature T_c = 75°C, and melting point T_m < -20°C.

To characterize the electro-optic performance, we filled JC-BP08 into an IPS cell with no surface alignment layer. Because JC-BP01 has a similar ε' value, we include it as benchmark for comparison. The IPS-8/12 cells we employed have ITO electrode width w = 8 µm, electrode gap g = 12 µm, and cell gap d = 7.3 µm. When heated to BP-I, the cells were cured under UV light (λ ~ 365 nm, intensity 8 mW/cm^2) for 15 min. For convenience, we call the two samples as PSBP-01 and PSBP-08. Our experiment was conducted at room temperature unless otherwise mentioned.

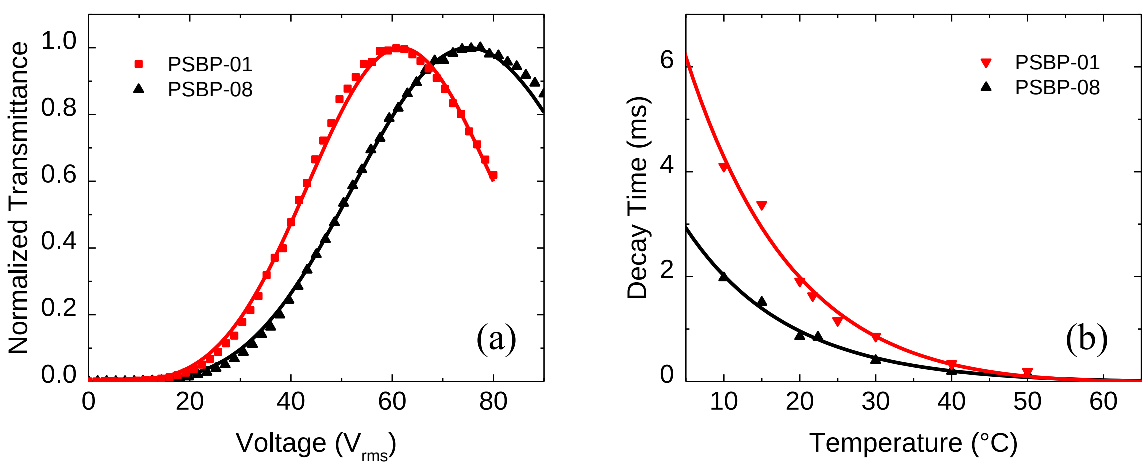

Figure 3-1 (a) VT curves at room temperature and (b) temperature dependent decay time of PSBP-01 and PSBP-08 at λ = 633 nm and frame rate = 240 fps. Dots are experimental data and lines are fitting curves.

Figure 3-1 depicts the measured voltage dependent transmittance (VT) curves and temperature dependent decay time of PSBP-01 and PSBP-08, respectively. Here, the transmittance is normalized to that of two parallel polarizers. We also fit the experimental VT curves with the extended Kerr effect model, in which the induced birefringence Δn_{ind} is related to the electric field E as [54]:

$$\Delta n_{ind} = \Delta n_s \left(1 - \exp\left[-\left(E / E_s\right)^2\right]\right), \tag{3-1}$$

where Δn_s stands for the saturated birefringence and E_s for the saturation electric field. As Figure 3-1(a) depicts, Equation (3-1) fits the measured VT curves of PSBP-01 and PSBP-08 well by TechWiz (SANAYI System). Through fittings, we found $\Delta n_s = 0.138$ and $E_s = 6.0$ V/μm for PSBP-08, and $\Delta n_s = 0.135$ and $E_s = 4.7$ V/μm for PSBP-01. Based on these parameters, we obtained Kerr constant $K = 6.1$ nm/V^2 for PSBP-08, and $K = 9.7$ nm/V^2 for PSBP-01. Our Kerr constant of PSBP-01 is somewhat smaller than that reported in [44], because our measurement is at a higher temperature. As Figure 3-1 depicts, PSBP-01 shows a lower V_p than PSBP-08 because of its larger Kerr constant, but its response time is > 2× slower than that of PSBP-08 at room temperature. This difference amplifies in the low temperature region. The difference between PSBP-01 and PSBP-08 mainly comes from the average elastic constant (k), which contributes to Kerr constant (K) and response time (τ) by the following equations [37,55]:

$$K \approx \frac{\Delta n \Delta \varepsilon P^2}{k \lambda \left(2\pi\right)^2}, \tag{3-2}$$

$$\tau \approx \frac{\gamma_1 P^2}{k \left(2\pi\right)^2}, \tag{3-3}$$

where Δn, $\Delta\varepsilon$, P, and γ_1 represent the birefringence, dielectric anisotropy, pitch length, and rotational viscosity of the BPLC composite, respectively, and λ is the wavelength. JC-BP01 has its advantage of large Kerr constant, so the low operation voltage makes it useful for general displays. However, to achieve a faster response time than JC-BP01, our JC-BP08 exhibits a larger

k, which helps to shorten the response time [Equation (3-3)] but its Kerr constant is somewhat compromised [Equation (3-2)]. The pitch length is also slightly adjusted from P = 412 nm for PSBP-01 to P = 376 nm for PSBP-08.

3.2.1 Gray-to-gray response time

PSBP-08 exhibits very fast gray-to-gray (GTG) response time. Table 3-1 lists the measured gray-to-gray (GTG) response time of PSBP-08 at room temperature *without* overdrive and undershoot voltages. The averaged GTG rise time is 0.9 ms and decay time is 1.0 ms. The slowest GTG response time (from gray level 1 to gray level 2) is 1.827 ms. Such a fast response time certainly helps diminish motion blur.

Table 3-1 Measured response time of PSBP-08 between different grey levels (1-8).

	Rise time (ms)								
Decay time (ms)		1	2	3	4	5	6	7	8
	1		1.827	1.775	1.490	1.476	1.330	1.129	0.560
	2	0.258		1.028	1.197	1.096	1.035	0.862	0.326
	3	0.317	0.879		0.935	1.024	1.202	0.988	0.357
	4	0.351	0.831	0.602		0.868	0.821	0.749	0.350
	5	0.415	0.798	1.103	1.393		0.723	0.683	0.324
	6	0.445	0.884	0.959	1.245	1.607		0.632	0.292
	7	0.546	1.003	1.124	1.274	1.231	1.183		0.246
	8	0.846	1.525	1.393	1.330	1.413	1.359	1.482	

3.2.2 Wavelength and frequency effects

For a given PSBP composite, Δn_s governs its optical response, e.g. transmittance, while E_s determines its operation voltage. Both Δn_s and E_s influence Kerr constant by [51]

$$K = \Delta n_s / \left(\lambda E_s^{\,2} \right). \tag{3-4}$$

Equation (3-4) implies that to lower the operating voltage (i.e. larger Kerr constant), higher Δn_s, shorter wavelength and lower E_s are preferred.

Figure 3-2 depicts the wavelength effect of PSBP-08. In Figure 3-2(a), we fixed E_s = 6.0 V/μm at 240 fps and fitted the VT curves at the specified wavelengths. The obtained Δn_s values are plotted in Figure 3-2(b). We further fitted the Δn_s dispersion with following equation [56]:

$$\Delta n_s = G \frac{\lambda^2 \lambda^{*2}}{\lambda^2 - \lambda^{*2}}, \tag{3-5}$$

and obtained the proportionality constant G = 2.07 μm^{-2} and the mean resonance wavelength λ^* = 239 nm. From Equation (3-5), we find Δn_s = 0.146 at λ = 550 nm for PSBP-08.

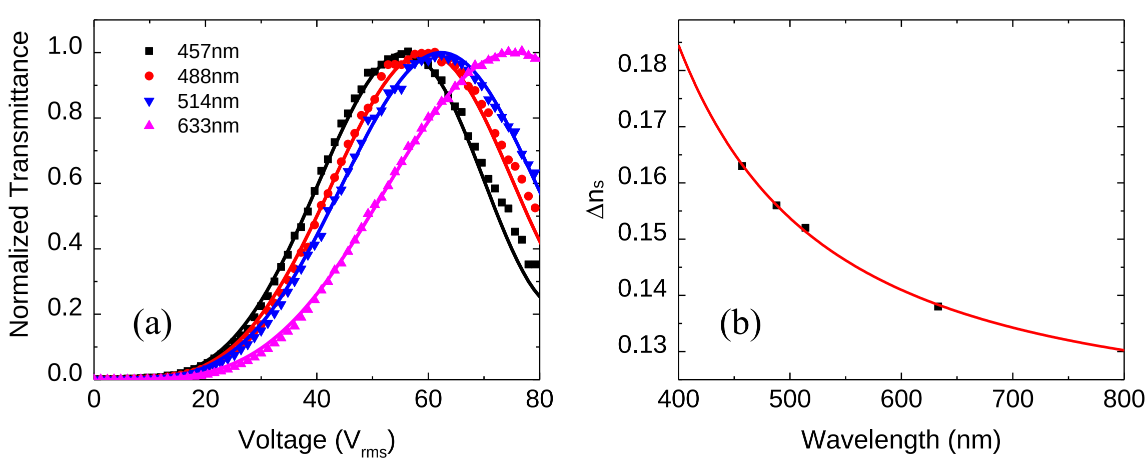

Figure 3-2 (a) Measured and fitted VT curves of PSBP-08 at the specified wavelengths, 240 fps and room temperature. Dots are measured data; lines are fitting curves with Equation (3-1) by fixing E_s = 6.0 V/μm. (b) Dispersion of Δn_s for PSBP-08. Dots are results obtained from (a) and red line represents the fitting with Equation (3-5).

High frame rate helps to mitigate motion blur, but the tradeoff is increased electronic power consumption. Figure 3-3(a) depicts the frequency dependent VT curves. As the frequency (f_{AC}) increases from 60 Hz to 2 kHz, V_p increases gradually. To fit each VT curve, we fixed $\Delta n_s = 0.138$ (for $\lambda = 633$ nm) and obtained different E_s values. Based on the Δn_s and E_s values, we calculated the Kerr constant as plotted in Figure 3-3(b). Next, we fitted the experimental data with following extended Cole-Cole equation [51]:

$$K(f) = K_\infty + (K_s - K_\infty)\frac{1+\left(\frac{f_{AC}}{f_r}\right)^{1-\alpha}\sin\frac{1}{2}\alpha\pi}{1+2\left(\frac{f_{AC}}{f_r}\right)^{1-\alpha}\sin\frac{1}{2}\alpha\pi+\left(\frac{f_{AC}}{f_r}\right)^{2(1-\alpha)}}. \quad \textbf{(3-6)}$$

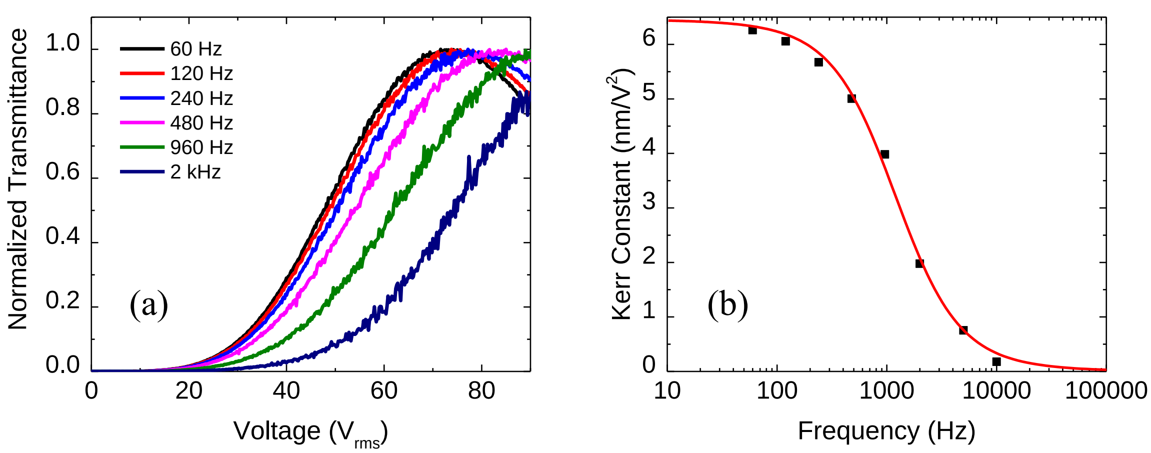

Figure 3-3 (a) Measured frequency (f_{AC}) dependent VT curves of PSBP-08 at λ = 633 nm and room temperature. (b) Frequency dependent Kerr constant of PSBP-08. Black dots are the extracted data from (a), while red line represents fitting with Equation (3-6).

Through fittings, we find static Kerr constant $K_s = 6.5$ nm/V^2, high frequency Kerr constant $K_\infty = 0$, Debye relaxation frequency $f_r = 1.2$ kHz, and $\alpha = 0.13$. For comparison, $f_r = 1.3$ kHz for PSBP-01 [51]. Since PSBP-08 has a similar ε' to PSBP-01, their f_r values are also comparable. As

Figure 3-3(b) depicts, Kerr constant decreases gradually as the frequency increases. At f_{AC} = 120 Hz (frame rate 240 fps), the Kerr constant slightly decreases to 6.1 nm/V^2.

3.2.3 Charging issue for high dielectric constant BPLCs

Fast capacitor charging time plays a key role for high frame rate and high-resolution display devices. In 2013, Haseba, et al. [48] used PSBP-06 to demonstrate that LC with a larger dielectric constant (ε') needs a longer time to be fully charged. A higher ε' LC implies to a larger capacitor, as a result, it requires a longer time to accumulate the electric charges. Similar to Kerr constant, the dielectric constant of BPLC declines as the driving frequency increases. A short (typically 20-μs) DC voltage from TFT contains some high frequency components. From Figure 3-3(b), during such a short charging time, the corresponding ε' value is very small. Since the following frame time is much longer than the charging time, the voltage-holding frequency is much lower than the charging frequency. At the beginning of open circuit, the working frequency drops quickly from the high charging frequency to the low voltage-holding frequency, thus ε' and the capacitance increase instantly, resulting in a low charged-in voltage. Nematic LCs do not suffer such problem because their ε' is small and insensitive to the driving frequency as long as f_{AC} < 100 kHz.

Figure 3-4 is an illustration of the slow charging time and low voltage holding ratio issues of a BP LCD. In Figure 3-4(a), let us assume the applied voltage is V_0 = 10 V and charging time t_c = 16 μs. Because the BPLC has a large capacitance, it requires much longer time to reach 10 V. With such a short charging time, the charged-in voltage V_i is about 4.2 V, which is much lower than V_0. After a holding time of t_h = 4.2 ms [240 fps], the held voltage decreases to V_h. Therefore, two parameters determine the electrical performance of a BP LCD: 1) charging time: it is related to ε' and f_r, which indicates how ε' changes with frequency; 2) *VHR* defined as V_h / V_i: it represents how well the voltage is held in a given frame time. Our PSBP-08 has a moderate ε', its charging time is about 250 μs, which is still more than 10× longer than that of a conventional nematic LC. But once charged, its *VHR* reaches 99.4% at 25°C and 93.2% at 60°C. The high *VHR* is because JC-BP08 consists of mainly fluorinated multi-ring compounds [52]. Fluorinated liquid crystals exhibit a high resistivity, which leads to a large *VHR* [57], and have been widely used in TFT LCDs.

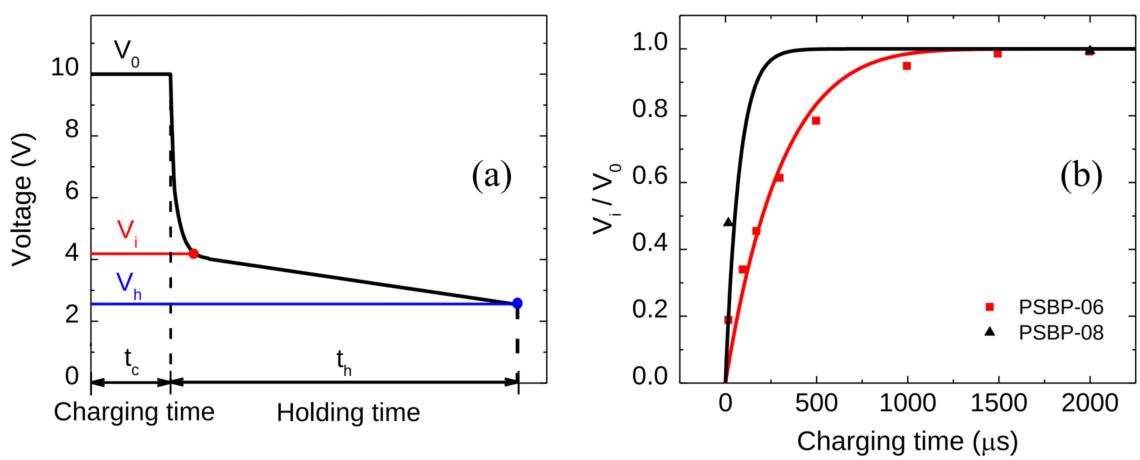

Figure 3-4 (a) Schematic illustration of the charged-in voltage and voltage holding ratio. t_c, t_h, V_0, V_i and V_h stand for charging time, holding time, applied voltage, charged-in voltage and held voltage, respectively. (b) Charging time dependent V_i / V_0, where dots are experimental data and lines are fitting curves according to Equations (3-7)-(3-9).

In principle, we should compare the charging issues of our PSBP-08 with PSBP-01 directly. However, there are no such data available for PSBP-01. Instead, we found the experimental data of PSBP-06 reported in [48]. Figure 3-4(b) shows the measured V_i / V_0 of PSBP-06 (red dots) and our measured PSBP-08 (black triangles). PSBP-06 has a very large ε' (~ 200), so its required charging time is about 1.5 ms. To understand the slow charging phenomenon, we propose following equations:

$$V_i / V_0 = 1 - \exp\left(-t_c / t_0\right), \tag{3-7}$$

$$t_0 = b \cdot \varepsilon'\left(f_{AC}\right), \tag{3-8}$$

$$f_{AC} = \frac{1}{2t_c}, \tag{3-9}$$

where t_c is the charging time (a variable), t_0 is a characteristic charging time, which is linearly proportional to ε' by a constant b, and f_{AC} is the driving frequency (= 0.5 × frame rate). First, we fit the red dots in Figure 3-4(b) with Equations (3-7)-(3-9), as the red line shows, and obtain b = 1.704. The agreement between model and experiment is very good. Next, we use the same b value to fit our PSBP-08 data *without* any adjustable parameter. Results are shown by the black line. Again, the agreement is good, although we have only two data points. Therefore, our model is validated experimentally. As shown in Figure 3-4(b), PSBP-06 has a huge ε', which is desirable for lowering the operation voltage, but the required charging time is 1.5 ms. By contrast, PSBP-08 has a smaller ε' so that its required charging time (~ 250 μs) is shortened by 6×, which is easier to be addressed by the pre-charging method [49,50].

3.3 Device performance

Although we have overcome the charging issues, the high driving voltage is PSBP-08's Achilles heel. Our target is to lower the operation voltage to 15 V to enable single-TFT addressing, while keeping a reasonably high transmittance, say > 70%. In this Section, we perform device simulation using PSBP-08 in some reported protrusion structures.

3.3.1 Protrusion electrode for low driving voltage

In 2009, Rao, et al. [42] proposed a protruded electrode structure for lowering the operation voltage. This approach is proven to be quite effective. Several groups have fabricated such structures [40,41,58], especially in 2015 AUO demonstrated such protrusion electrodes in a 10" BPLC prototype [41]. The peak transmittance is over 75%, but the operation voltage is 32 V so that two TFTs per pixel are required. High V_p increases the power consumption while two TFTs reduce the aperture ratio and optical efficiency.

For the protrusion structure, fabrication technique limits the best performance that can be achieved. As Figure 3-5(a) depicts, to lower V_p, we could decrease the protrusion gap (g) to increase the electric field intensity between two protrusions, or increase protrusion height (h) for the incoming light to accumulate more phase retardation. Nevertheless, narrower gap demands a smaller protrusion width (w) to keep high transmittance, since the area above the protrusion is a dead zone. Under such a condition, tall and thin protrusion is favored, but of course, they are more challenging to fabricate. Several other electrode structures have been proposed, but the fabrication is a limiting factor in practice [59-61]. In 2012, Yamamoto, et al. proposed and fabricated a triangular electrode structure (Figure 3-5(a)) to improve contrast ratio [62,63], whose protrusion height is h = 2.14 μm and width is w = 1.32 μm.

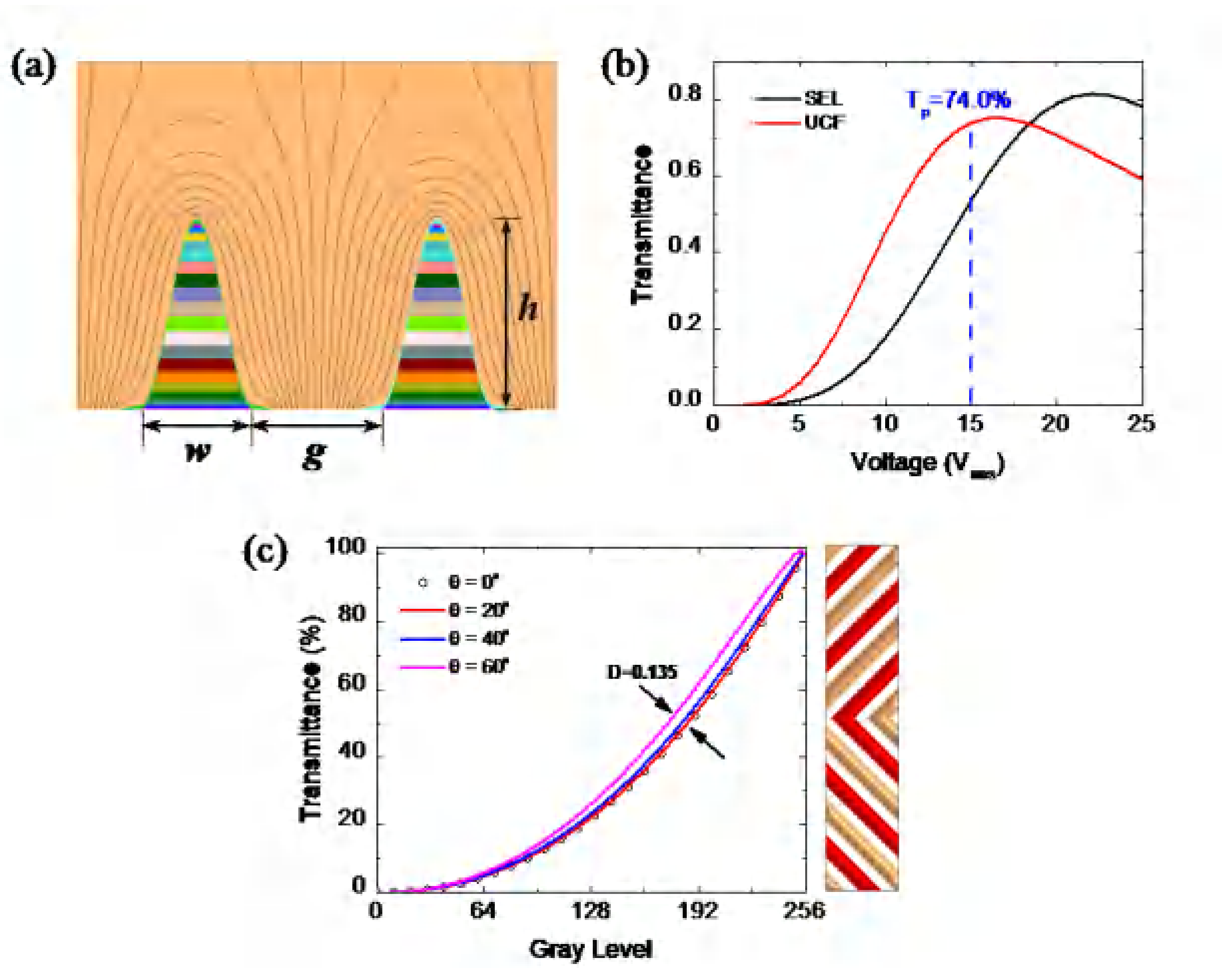

Figure 3-5 (a) The triangular electrode structure used in simulation, where h = 2.14 µm, w = 1.32 µm, cell gap d = 4 µm, and the ITO tails beside the protrusion are kept for applying voltage. (b) Simulated VT curves of PSBP-08 (λ = 550 nm, frame rate = 240 fps) using the triangular electrode structure. The black and red lines refer to using the original protrusion gap g = 2.68 µm and using our optimized protrusion gap g = 1.5 µm, respectively. (c) Viewing angle dependence of gamma curves for film-compensated two-domain triangular electrode structure along the most severe gamma shift direction (ϕ = 230°). The right picture shows the two-domain structure configuration. Red and orange denote common and pixel electrodes, respectively.

3.3.2 Performance of PSBP-08 on protruded electrodes

Here, we study the performance of our PSBP-08 using the protruded triangular electrodes. In Figure 3-5(a), a ridge protrusion is deposited on the bottom substrate, then ITO stripes are sputtered onto the ridge protrusion. Except for the protrusion gap, the parameters used in our simulation are kept the same as those prototypes reported in [62,63], so that the fabrication process should also be the same: h = 2.14 μm, w = 1.32 μm, cell gap d = 4 μm; the ITO tails beside the protrusion are for applying voltage. The black line in Figure 3-5(a) shows the simulated VT curve using the experimental protrusion gap g = 2.68 μm. The peak transmittance is ~ 82% at 22 V. To lower V_p to 15 V, we reduce the protrusion gap to g = 1.5 μm, which is still comparable to the dimension of protrusion width w = 1.32 μm. As the red line shows in Figure 3-5(b), we can achieve 74% transmittance at 15 V. Thus, PSBP-08 is a promising candidate for practical applications.

For display applications, gamma shift is another important parameter. The well-known example is multi-domain vertical alignment for LCD TVs. In order to suppress gamma shift, 12 domains are often employed. As a result, the transmittance is greatly reduced because the domain walls block the light.

Here, we investigate the gamma shift of BP LCDs. It has been reported that a single-domain BPLC exhibits greyscale inversion, and to suppress grayscale inversion and widen viewing angle, two-domain structure and biaxial compensation film are needed [64]. We calculated the gray level (GL, 0-255) from transmittance (T) by $T = (\mathrm{GL} / 255)^{2.2}$. The gamma curves along the most severe gamma shift direction ($\varphi = 230°$) are plotted in Figure 3-5(c). We find the off-axis image distortion index $D(\theta, \varphi) = 0.135$. From previous studies [65,66], as long as $D < 0.2$ the gamma shift is unnoticeable to the human eye. Therefore, for BP LCDs we only need two domains to achieve wide-view and distortion-free off-axis images. By merely using two domains, the effective transmittance should remain high. Moreover, since we are using IPS structure, which is insensitive to the cell gap, the BP LCD should work well for touch panels.

3.4 Conclusion

Our new PSBP-08 exhibits following outstanding features: 1) Its fast response time helps mitigate motion blur. The average and slowest GTG response time are respectively < 1 ms and < 2 ms. 2) Its *VHR* is adequate to support active matrix operation. 3) Its blue phase temperature range (from -20°C to 75°C) is adequate for indoor applications. 4) Its average dielectric constant is 87, which is still below the upper limit for bootstrapping driving. Thus, it facilitates the signal capacity charging and reduces the data input time. 5) Using the triangular electrode structure, PSBP-08 can achieve 74% transmittance at 15 V, which enables single-TFT driving. 6) With two-domain structure, our BP LCD offers indistinguishable gamma shift and wide viewing angle. A linear relationship between charging time and ε' is proposed and validated by experiment.

CHAPTER 4 SUBMILLISECOND NEMATIC LIQUID CRYSTALS

4.1 Introduction

In this chapter, we report new nematic LC materials with submillisecond response time, which has been published in [67]. Liquid-Crystal-on-Silicon (LCoS) is a competitive candidate for augmented reality (AR) head-mounted displays [68-71] for its attractive features of high luminance (> 40 000 cd/m^2) [69], high resolution density (> 4000 ppi) [70], high fill factor (> 90%), low operation voltage (< 6 V) and compact size (< 1.5 inch). It can realize both phase modulation for holographic displays [72,73] and amplitude modulation for image projections [74-76]. For the phase modulation, a minimum 2π-phase change is required. Phase-only LCoS is receiving increasing attention for the ability of encoding high-quality 3D image information. For the amplitude modulation, 1π phase retardation and high contrast ratio are critically needed, making reflective 90° mixed-mode twist nematic (MTN) and vertical alignment (VA) LCoS panels common choices. Most commercially available LCD AR devices are based on MTN LCoS panels, such as Google Glass, Microsoft HoloLens and Magic Leap One. As a reflective device, LCoS can be combined with either a conventional light source or a mLED/μLED local dimming backlight for contrast ratio enhancement.

As discussed in Chapter 2, fast pixel response time is highly desirable for motion blur suppression. Polymer network LCs [77], polymer-stabilized short-pitch cholesteric LCs [78] and ferroelectric LC [79] can offer submillisecond response time. But the first two polymer-stabilized approaches need a high voltage that exceeds the sustainability of LCoS backplane. On the other hand, due to the bi-stable behavior of ferroelectric LC, digital driving is required for high-quality image reproduction, which in turn raises power consumption. In comparison, nematic LC can provide superior image quality with low operation voltage, whose drawback is relatively slow response time (5 ~ 10 ms). In order to acquire fast response time, one promising strategy is to employ high birefringence ($\Delta n > 0.25$) LC with thin cell gap. Whereas, high Δn LCs are vulnerable to high melting temperature (terphenyl type [80]) or the UV stability is compromised (NCS-tolane type [81,82]). Therefore, the development of high Δn LC materials with low viscosity, modest dielectric anisotropy and reasonably high resistivity ($>10^{12}$ Ω·cm) is urgently needed.

In this chapter, we report three nematic LC mixtures optimized for LCoS. When used in a reflective 90° MTN cell for amplitude modulation, their high birefringence ($\Delta n \sim 0.25$ at 25°C, 550 nm) and low rotational viscosity ($\gamma_1 \sim 130$ mPa·s) jointly contribute to submillisecond response time (0.90 ms). Their relatively large dielectric anisotropy ($\Delta\varepsilon > 6.6$) helps to lower the operation voltage. At 5 V, high contrast ratio (2097:1) is experimentally obtained.

4.2 Material characteristics

We use LC-1, LC-2 and LC-3 to denote the three new LC mixtures, developed by DIC Corporation. Their physical properties were characterized at temperature T_{LC} = 25°C and results are summarized in Table 4-1. We measured the melting temperature (T_m) and clearing temperature (T_c) by Differential Scanning Calorimetry (DSC, TA instruments Q100). The wide nematic range (< -35°C ~ 85°C) satisfies the requirement for most AR applications. The dielectric constants were measured with a multi-frequency LCR meter HP-4274. The reasonably large $\Delta\varepsilon$ contributes to a low operation voltage, which is desirable for head-mounted display devices. The rotational viscosity γ_1 and [splay, twist, bend] elastic constants [K_{11}, K_{22}, K_{33}] were measured through transient current method by autronic-MELCHRS LCCS107. The low viscosity (γ_1 ~ 130 mPa·s) helps reduce the response time effectively. For active matrix displays, the LC resistivity should be higher than 10^{13} Ω·cm, while for LCoS it can be reduced to 10^{12} Ω·cm because of the higher frame rate. The resistivity of our three LC mixtures satisfies this requirement.

Table 4-1 Measured physical properties of LC-1, LC-2, and LC-3 at 25°C.

LC mixture	LC-1	LC-2	LC-3
T_c (°C)	86.5	84.9	85.7
T_m (°C)	< -40	-35.4	< -40
Δn @550 nm	0.251	0.247	0.25
$\Delta\varepsilon$ @1 kHz	6.68	9.1	6.75
$\varepsilon_\perp$ @1 kHz	3.5	3.83	3.41
γ_1 (mPa·s)	133	130	123
K_{11} (pN)	12.1	11.7	12.2
K_{22} (pN)	7.6	6.8	7.4
K_{33} (pN)	15.4	14.4	14.6
γ_1 / K_{11} (ms/µm2)	11.0	11.1	10.1
Resistivity (Ω·cm)	1.6×10^{12}	7.0×10^{11}	8.8×10^{11}

4.2.1 Birefringence

Birefringence determines the cell gap, which in turn affects the response time. To measure Δn, we filled each LC mixture into a homogeneous cell with cell gap d = 5 µm. The pretilt angle of the rubbed polyimide alignment layers is about 3°. We sandwiched each cell between crossed polarizers and activated it with a 1-kHz square-wave AC voltage. The birefringence was calculated from the measured phase retardation [84]. Figure 4-1(a) depicts the temperature dependent birefringence at λ = 632.8 nm (He-Ne laser). The sample temperature was controlled by a Linkam heating stage through a temperature programmer TMS94. The extrapolated birefringence Δn_0 at temperature T_{LC} = 0 K and the exponent β were obtained by fitting experimental data with equation [85]:

$$\Delta n = \Delta n_0 S = \Delta n_0 \left(1 - T_{LC} / T_c\right)^{\beta} . \qquad \textbf{(4-1)}$$

To be noticed, in Equation (4-1), T_{LC} and T_c should be in unit Kelvin. The fitting results are listed in Table 4-2.

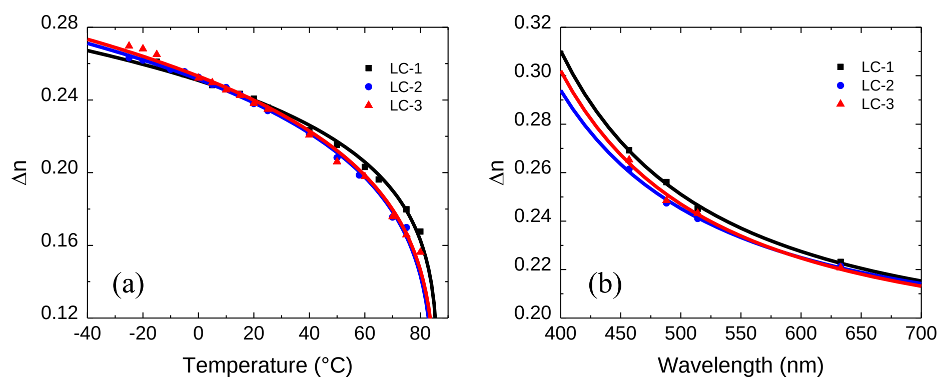

Figure 4-1 (a) Temperature dependent birefringence at λ = 633 nm, f_{AC} = 1 kHz. (b) Dispersion of birefringence at f_{AC} = 1 kHz, T_{LC} = 40°C. Dots are measured data; lines in (a) and (b) are fitting curves with Equation (4-1) and Equation (4-2), respectively.

For a working LCoS device, its operating temperature is about 40°C due to the thermal effects of backplane and the light source [86]. Therefore, we focus our studies at T_{LC} = 40°C. To measure the wavelength dispersion, in experiment we used a He-Ne laser (λ = 632.8 nm) and a tunable Argon ion laser (λ = 457 nm, 488 nm and 514 nm). Results are plotted in Figure 4-1(b). The single-band birefringence dispersion equation [56] was used for fitting:

$$\Delta n = G \frac{\lambda^2 \lambda^{*2}}{\lambda^2 - \lambda^{*2}} , \qquad \textbf{(4-2)}$$

where G is a proportionality constant and λ^* is the mean resonance wavelength. At λ = 633 nm and T_{LC} = 40°C, the Δn of [LC-1, LC-2, LC-3] is [0.2233, 0.2213, 0.2207], respectively. The obtained G & λ^* values are also listed in Table 4-2.

Table 4-2 Fitting parameters obtained through Equations (4-1)-(4-3).

LC mixture	Δn_0	β	G @40°C (μm-2)	λ^* @40°C (μm)	A (ms/μm^2)	E_a (meV)
LC-1	0.318	0.167	2.96	0.251	3.00×10^{-5}	315.8
LC-2	0.334	0.197	3.32	0.239	5.36×10^{-6}	355.1
LC-3	0.338	0.202	3.05	0.247	1.80×10^{-6}	377.4

4.2.2 Visco-elastic coefficient

We also measured the transient decay curves of these LC mixtures and obtained the temperature dependent visco-elastic coefficient γ_1 / K_{11}, as the dots presented in Figure 4-2. The solid lines represent fittings with following relation [87]:

$$\frac{\gamma_1}{K_{11}} = A\frac{\exp\left(E_a / k_B T_{LC}\right)}{\left(1-T_{LC} / T_c\right)^{\beta}}. \qquad \textbf{(4-3)}$$

Here, A, E_a, and k_B stand for the proportionality constant, Boltzmann constant, and activation energy, respectively. The fitting parameters are also included in Table 4-2. From Figure 4-2 and Equation (4-3), we can see that γ_1 / K_{11} decreases dramatically as the temperature increases. At T_{LC} = 40°C, the γ_1 / K_{11} of [LC-1, LC-2, LC-3] is [5.8, 6.0, 5.15] ms/μm^2, respectively.

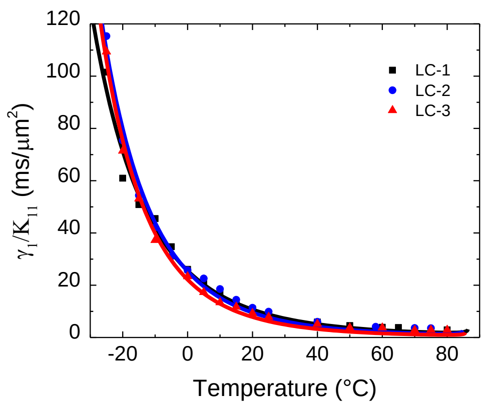

Figure 4-2 Temperature dependent visco-elastic coefficient at λ = 633 nm and f_{AC} = 1 kHz. Dots are measured data and lines are fitting curves with Equation (4-3).

4.2.3 Photostability

During the fabrication process, an LCoS panel is usually exposed to UV light in order to seal the filling hole. Such a UV exposure could damage the LC mixture or the alignment layer, depending on the photostability of employed LC and alignment materials. If an LCoS is using a low birefringence LC and inorganic alignment layers, such as silicon-dioxide (SiO_2), then the photostability is not a concern [88]. However, to increase birefringence while keeping a low viscosity, a small percentage (5 ~ 10 wt.%) of tolane compounds is often added to the mixtures, which is sensitive to UV light.

To investigate photostability, we chose LC-1 as an example for this study because it has the widest nematic range and highest resistivity among the three samples listed in Table 4-1. In experiment, we injected LC-1 into two 9.3-μm-thick homogeneous cells with SiO_2 alignment layer. We measured the birefringence and visco-elastic coefficient of the samples after UV exposure and recorded the changes in Figure 4-3. Figure 4-3(a) depicts the measured photo-stability of LC-1 at λ = 365 nm. As the UV dosage increases, Δn decreases and γ_1 / K_{11} increases slightly. Compared to the initial value, Δn decreases 4.1% whereas γ_1 / K_{11} increases 4.3% after 20 J/cm^2 of UV exposure and then saturates. In LCD industry, to seal the LC filling hole, a λ = 365 nm UV light with dosage of ~10 J/cm^2 is commonly used. This indicates that LC-1 is relatively UV-robust, considering its high birefringence and low visco-elastic constant. However, to prevent photo-degradation, we still recommend blocking the LC area during UV exposure. An alternative choice is to use a longer wavelength UV, say λ = 385 nm [89]. From the measured photo-stability results in Figure 4-3(b), even after 120-J/cm^2 of UV exposure at λ = 385 nm, its Δn only drops by 3.1% as compared to the initial value, while γ_1 / K_{11} fluctuates within 1.6% variation.

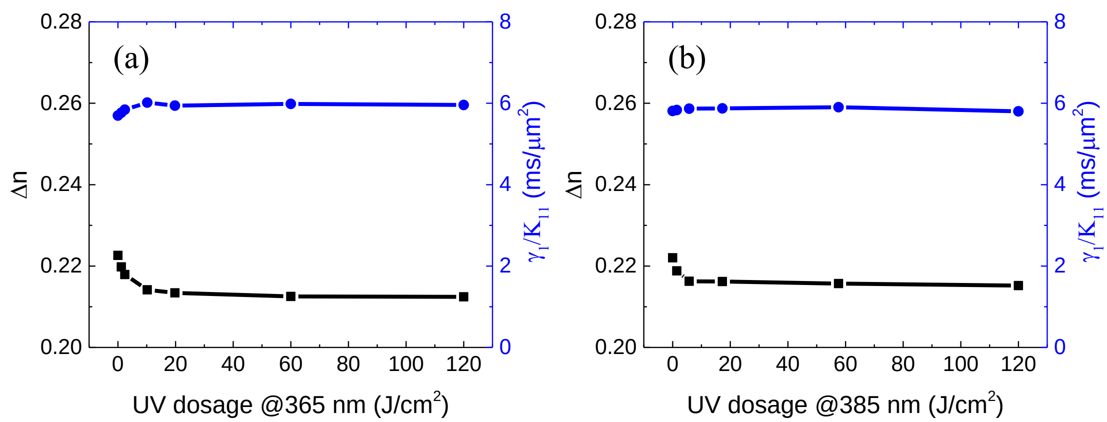

Figure 4-3 Measured photo-stability of LC-1 with an UV LED at (a) 365 nm and (b) 385 nm. Probing laser beam: λ = 633 nm. Measurement temperature: 40°C. Black rectangles denote birefringence and blue circles denote visco-elastic constant.

4.3 2π phase modulation in homogeneous-aligned cells

4.3.1 Voltage dependent phase change (V-Φ) curves

To simulate the performance in a real LCoS device, we filled each LC mixture into a transmissive homogeneous cell with cell gap $d \approx 3.4$ µm. This is the thinnest cell gap we have in our labs. Its phase retardation is equivalent to that of a reflective 1.7-µm-thick cell, because of the doubled optical path. Using the physical parameters measured at λ = 633 nm and T_{LC} = 40°C, we simulated the voltage dependent transmittance (V-T) curves by a commercial LCD simulator DIMOS 2.0. Figure 4-4 compares the V-Φ curves converted from the measured V-T curves (dots) and the simulated V-T curves (lines). The simulation agrees well with experiment.

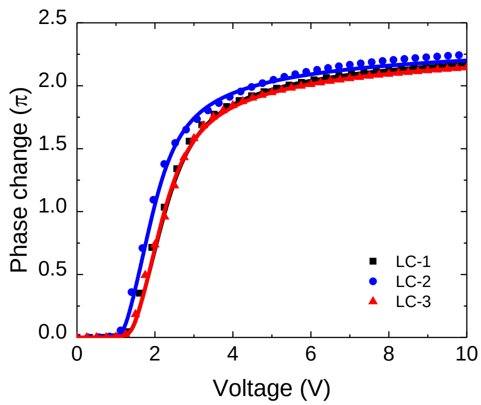

Figure 4-4 Measured and simulated V-Φ curves at T_{LC} = 40°C, λ = 633 nm and f_{AC} = 1 kHz. Dots are measured data in transmissive homogenous cells with d = 3.4 µm; lines are simulated curves in reflective homogenous cells with d = 1.7 µm.

4.3.2 Response time

The response time (τ) of an LC cell is proportional to d^2. Thus, the response time of our 3.4-µm transmissive cell is expected to be 4× longer than that of a 1.7-µm-thick reflective cell. Table 4-3 compares the measured and simulated response times. For each LC mixture, the first row represents the measured result of the transmissive cell; the second row is the extrapolated result for the reflective LCoS, where the cell gap is half and the response time is one-fourth of the transmissive cell, and the third row is the simulated result of a reflective cell. Good agreement is achieved between experiment and simulation.

Table 4-3 Response time of measured, extrapolated and simulated results at T_{LC} = 40°C, λ = 633 nm and f_{AC} = 1 kHz.

LC mixture	Type		d (μm)	$V_{2\pi}$ (V)	τ_{on} (ms)	τ_{off} (ms)	$\tau_{on} + \tau_{off}$ (ms)
LC-1	Measured	Transmissive	3.40	5.38	1.23	7.82	9.05
	Extrapolated	Reflective	1.70	5.38	0.31	1.95	2.26
	Simulated		1.66	5.38	0.37	2.21	2.58
LC-2	Measured	Transmissive	3.44	4.57	1.44	8.15	9.59
	Extrapolated	Reflective	1.72	4.57	0.36	2.04	2.40
	Simulated		1.67	4.57	0.40	2.34	2.74
LC-3	Measured	Transmissive	3.39	5.78	0.96	6.65	7.61
	Extrapolated	Reflective	1.69	5.78	0.24	1.66	1.90
	Simulated		1.65	5.78	0.28	2.00	2.28

Table 4-4 Selected nine phase levels between 0 and 2π, and the corresponding operation voltage of LC-1. The listed data are obtained from Figure 4-4.

Phase level	1	2	3	4	5	6	7	8	9
Phase change (π)	0	0.25	0.5	0.75	1	1.25	1.5	1.75	2
Voltage (V)	0	1.52	1.72	1.95	2.21	2.46	2.77	3.42	5.38

Table 4-5 Measured PTP response time of LC-1 in a transmissive homogenous cell with d = 3.4 μm. Note: the LCoS response time with d = 1.7 μm is 4× faster than the data shown here.

	Rise time (ms)									
Decay time (ms)		1	2	3	4	5	6	7	8	9
	1	*	44.47	25.83	17.02	12.29	9.16	6.78	3.55	1.23
	2	8.27	*	17.34	13.07	10.06	7.77	5.56	3.01	1.03
	3	7.75	21.36	*	11.76	9.12	6.81	4.60	2.58	0.91
	4	7.82	20.31	14.40	*	8.07	6.05	3.61	2.32	0.82
	5	7.64	17.77	13.57	9.18	*	5.52	3.39	2.15	0.79
	6	7.57	13.97	11.95	8.51	6.68	*	3.35	2.04	0.78
	7	7.56	14.90	10.89	7.82	6.29	4.37	*	2.10	0.80
	8	7.57	15.24	10.39	7.73	6.33	4.89	4.04	*	0.77
	9	7.82	14.88	10.15	7.83	6.56	4.76	3.92	2.10	*

In an AR device, the LCoS panel is expected to tune the phase change continuously from 0 to 2π. Here, we selected nine phase levels to represent the full phase tuning range. By measuring the response time between each two levels, we can obtain a phase-to-phase (PTP) response time chart. Still using LC-1 as the example, Table 4-4 lists the representative phase levels and the corresponding operation voltage of the 3.4-μm-thick homogenous cell, while Table 4-5 summarizes the measured PTP response time *without* overdrive/undershoot circuitry. The measured average PTP response time is 8.32 ms. Therefore, for $V_{2\pi}$ = 5.38 V, the extrapolated PTP response time for a reflective LCoS panel is 2.08 ms, which enables 240-fps refresh rate for field-sequential-color (FSC) displays and color breakup mitigation [90,91].

4.3.3 New driving method on a full-color phase-only SLM device

After validating the reliability of our simulation, we simulated the V-Φ curves of LC-1 for RGB colors. From Figure 4-1(b) and Equation (4-2), the Δn at T_{LC} = 40°C and λ = [448 nm, 524 nm, 638 nm] are [0.2739, 0.2437, 0.2220]. These values are the wavelengths of three laser diodes employed in Microsoft's LCoS-based AR prototypes [72]. Either for color filter-type or for FSC-type LCoS, the cell gap for RGB colors should be the same since only one panel is utilized. In simulation, the cell gap was set at d = 1.716 μm to ensure $V_{2\pi} \leq 5$ V works for all three colors. As demonstrated in Figure 4-5, the red color with the longest λ and the lowest Δn has the highest $V_{2\pi}$ = 5 V. For green and blue colors, more than 2π phase change can be obtained within 5 V. Thus, we can choose a preferred 2π phase range to use for the green and blue colors. Here we denote V_1 and V_2 as the initial and final voltage of the selected 2π phase range. Here, V_2 is higher than V_{th}

(threshold voltage), but V_1 can be higher or lower than V_{th}. Under such condition, The LC rise time and decay time depend on the V_1 and V_2 as follows [92]:

$$\tau_{on} = \frac{\tau_0}{(V_2 / V_{th})^2 - 1}, \quad \textbf{(4-4)}$$

$$\tau_{off} = \frac{\tau_0}{\left|(V_1 / V_{th})^2 - 1\right|}, \quad \textbf{(4-5)}$$

where τ_0 (= $\gamma_1 d^2$ / $K_{11}\pi^2$) is the free relaxation time, i.e. V_1 = 0. From Equations (4-4) and (4-5), the response time near V_{th} is slow. If we set V_1 = 0 for the blue wavelength, then its V_2 is close to V_{th}, resulting in slow rise time, as Table 4-6 shows.

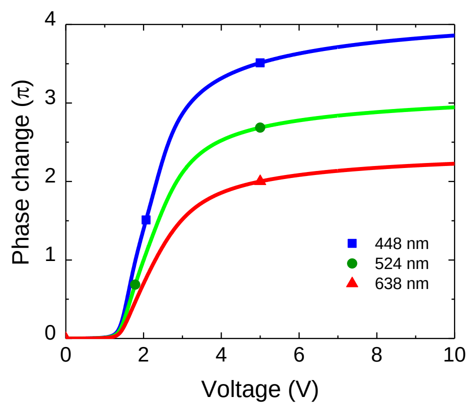

Figure 4-5 Simulated V-Φ curves of LC-1 for RGB colors at T_{LC} = 40°C in a reflective homogenous cell with d = 1.716 µm. Lines are V-Φ curves; dots mark the lower and upper limit of the 2π phase change range with V_2 = 5 V.

To overcome the above problem, we propose a new driving method to accelerate the response time of an LCoS panel intended for full-color operation. As demonstrated in Table 4-6, we manually set the same V_2 for all of the RGB colors, say V_2 = 5 V. The dots in Figure 4-5 mark the V_1 and V_2 in this design. For green and blue colors, V_1 > V_{th} is achieved. The simulated τ_{on} + τ_{off} in Table 4-6 shows the improvement over the driving method starting from V_1 = 0.

Table 4-6 Simulated response time of LC-1 at T_{LC} = 40°C in a reflective homogenous cell with d = 1.716 μm.

λ (nm)	Δn	V_1 (V)	V_2 (V)	τ_{on} (ms)	τ_{off} (ms)	$\tau_{on} + \tau_{off}$ (ms)
448	0.2739	(0.00	2.34	3.62	2.41	6.03)
		2.07	5.00	0.34	2.76	3.10
524	0.2437	(0.00	2.86	2.18	2.45	4.63)
		1.78	5.00	0.38	3.43	3.81
638	0.2220	0.00	5.00	0.51	2.48	2.99

A more dramatic improvement can be found in PTP response time because we intentionally shift V_1 and V_2 away from V_{th}. The slow PTP response time in the vicinities of V_{th} is replaced by the fast-response components at high voltage. Table 4-4 and Table 4-5 illustrate this concept. Here, V_{th} = 1.34 V is between phase level 1 and phase level 2. To get 1π phase change, we can either choose phase levels 1-5 or phase levels 5-9. Covering V_{th}, the average PTP response time between phase levels 1-5, e.g. the average value in the left top bolded rectangle in Table 4-5, is as slow as 14.86 ms. While for phase levels 5-9 above V_{th} (the right bottom bolded rectangle in Table 4-5), the average value is 3.58 ms, which is more than 4× faster than that of phase levels 1-5. For homogeneous-aligned cells, the average PTP response time is comparable with the sum of rise time and decay time. Table 4-5 confirms this phenomenon, where the average PTP response time 8.32 ms is comparable with $\tau_{on} + \tau_{off}$ = 9.05 ms. Using our new driving method, the response time ($\tau_{on} + \tau_{off}$) of all three primary colors is less than 4 ms, indicating < 4 ms average PTP response time for RGB colors. This enables 240-fps operation though a few slow-response phase levels are compromised.

4.4 Amplitude modulation with a 90° MTN cell

4.4.1 Voltage dependent transmittance (V-T) curve

To explore the performance of our new LC mixtures in projection displays, we fabricated a 90° MTN cell and filled LC-1 into it. A mirror was placed behind the cell to generate reflective mode. A polarizing beam splitter was employed functioning as two crossed polarizers. Again, we measured the V-T curve at T_{LC} = 40°C, λ = 633 nm and f_{AC} = 1 kHz. As depicted in Figure 4-6, the measured contrast ratio is 2097:1 at 5 V. The cell gap of the fabricated reflective 90° MTN cell was d = 1.32 μm, which is acceptable for mass production. If we control $d\Delta n$ ~ 240 nm, then the peak transmittance should be 88% [74].

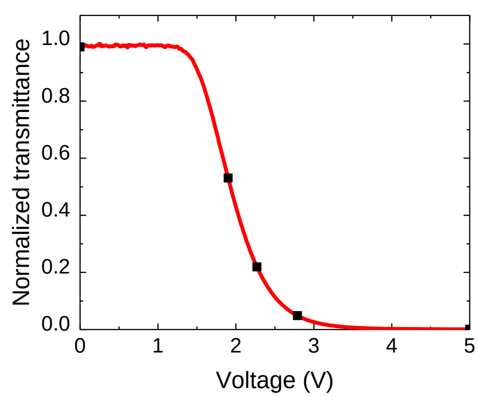

Figure 4-6 Measured VT curve in a reflective 90° MTN cell with d = 1.32 μm at T_{LC} = 40°C, λ = 633 nm and f_{AC} = 1 kHz. Dots mark the gray levels in Table 4-7.

4.4.2 Response time

As a result of the thin cell gap, submillisecond response time was achieved on this MTN cell. For 5-V operation, the [rise, decay] time is [0.136, 0.698] ms. The measured gray-to-gray (GTG) response time is summarized in Table 4-7. The gray level (GL, 0-255) was calculated from transmittance (T) by $T = (GL / 255)^{2.2}$. From Table 4-7 we can see, 0.90-ms average GTG response time is achieved *without* overdrive/undershoot circuitry. Except for one slowest GTG response time (2.40 ms from GL 255 to GL 192), all other GTG response time are less than 2 ms.

Table 4-7 Measured GTG response time of LC-1 in a 90° MTN cell with d = 1.32 μm.

	Rise time (ms)					
Decay time (ms)	GL	255	192	128	64	0
	255	*	2.401	1.363	0.648	0.136
	192	0.781	*	1.339	0.517	0.110
	128	0.762	1.916	*	0.493	0.123
	64	0.731	1.743	1.078	*	0.260
	0	0.698	1.619	0.825	0.476	*

4.5 Conclusion

We have developed three practical LC mixtures for LCoS-based augmented reality displays. The mixtures exhibit high birefringence to enable thin cell gap for fast response time, modest dielectric anisotropy for 5-V operation voltage, acceptable resistivity and UV stability, and wide nematic range. In experiment, these mixtures enable 2-ms response time in phase-only LCoS and submillisecond response time in MTN LCoS amplitude modulators, which is highly desirable for motion blur alleviation. Widespread applications of these mixtures for the emerging augmented reality displays are foreseeable.

CHAPTER 5 HIGH CONTRAST RATIO

5.1 Introduction

High dynamic range (HDR) displays require high peak luminance, uncompromising dark state and high contrast ratio [24-26]. This chapter concentrates on high contrast ratio (CR), and the content has been published in [19,21]. While emissive displays intrinsically exhibit high contrast ratio in darkroom, for conventional LCDs it is limited to 1000:1 ~ 5000:1 due to non-uniform LC alignment, scattering of the color filters, and diffraction from the pixelated electrodes. To boost contrast ratio, local dimming with spatially segmented backlight unit is an effective approach [21,27-30]. Each segment, the so-called local dimming zone, is controlled independently. With 10-bit backlight modulation, a high CR ~ 1 000 000:1 has been achieved [93].

However, challenges remain in conventional local dimming LCDs. The first challenge is in panel thickness. Conventional edge-lit LCDs feature thin profile, but the light guide plate is relatively thick implementing high-luminance large-area LEDs. Moreover, the local dimming performance in edge-lit LCDs is relatively limited [94]. On the other hand, although conventional local dimming direct-lit LCDs can provide better contrast ratio [95], the small amount of LEDs requires a long light propagation distance (i.e. thicker profile) for good backlight uniformity. In comparison, the small chip size and large number of mLEDs facilitate the light spreading in direct-lit LCDs so that it can effectively reduce panel thickness.

The second challenge of local dimming LCD is the annoying halo effect and clipping effect [29]. Halo effect is the light leakage from bright objects to adjacent dark areas. Clipping effect denotes the insufficient luminance in a local dimming zone when adjacent zones are dimmed.

Figure 5-1 schematically shows these two effects. The center of the local dimming zones are x_{zone} = 0, ±1, ±2, … with interval Δx_{zone} = 1. In Figure 5-1, only the center zone at x_{zone} = 0 is at peak luminance while the surrounding zones are dimmed. Ideally, the luminance of each zone should be uniform and independently controlled, as Figure 5-1(a) shows. However, in practice, the intensity of each local dimming zone is contributed by not only the aligned light source but also the light leakage from adjacent zones, as Figure 5-1(b) depicts. As a result, the intensity in the center zone is "clipped" to a lower level (purple area), and the light leaks to adjacent zones forming "halo" (yellow area). Afterward, a LC panel modulates the light from the backlight unit (red lines) to get finer details (blue lines). While the target light profile is plotted in Figure 5-1(c), the displayed image quality is degraded as Figure 5-1(d) shows. In order to suppress these two effects, a variety of local dimming algorisms have been developed from the basic "maximum", "average" methods, to the complex point spreading function (PSF) integrations [27,28]. In 2013, Burini et al. compared different algorisms and conducted optimization to find the best tradeoff point between halo and clipping effects with power constraint [96]. From the aspect of hardware, an infinitely high LC CR or pixel-level dimming could eliminate these two effects. Practically, increasing the number of local dimming zones could reduce the dark area affected by halo effect, e.g. the yellow area in Figure 5-1(b); a higher LC CR can effectively suppress the halo effect in the bright zones, e.g. the little light leakage in the central zone as indicated by the yellow area in Figure 5-1(d). However, the increasing zone number will lead to higher panel cost, and the improvement of LC CR is limited. "How many zones are required?" That is a question bothering panel manufacturers. In parallel, halo effect and clipping effect can be mitigated by reducing zone crosstalk. As the light is better confined in each designated local dimming zone, the luminance in each zone is less affected by adjacent areas. Whereas, strict local light confinement would compromise the spatial uniformity of the backlight.

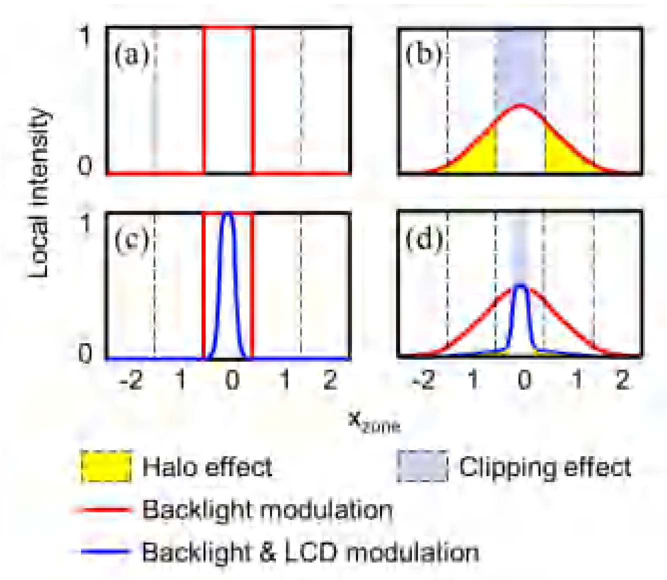

Figure 5-1 Schematic show of halo effect and clipping effect in local dimming LCDs: (a) ideal local dimming intensity profile; (b) practically obtainable local dimming intensity profiles (c) target intensity profile after LCD modulation; (d) practically obtainable intensity profile with halo effect and clipping effect.

In this chapter, we develop a simplified model for mLED-LCD system. After validating our model with experimental measurements, we use this model to optimize mLED-LCD system for halo effect and clipping effect suppression. We demonstrate how to design a mLED-LCD panel with unnoticeable halo effect and clipping effect. Quantitatively, we provide the required number of local dimming zones for given LC CRs. We show how the light profile of each local dimming zone affect the final display performance.

5.2 Device modeling

5.2.1 Modeling of mini-LED backlit LCD system

A schematic of mLED-LCD system is shown in Figure 5-2. Light is emitted from mLED chips. A diffuser is put above the mLED chips to spread the light for good spatial uniformity. The distance between mLED, diffuser and LC panel, as well as the diffuser scattering strength need to be optimized so that the outgoing light is spatially uniform before entering the LC layer. Above the diffuser is a LC panel. The gray level of each LC pixel is controlled by a thin-film-transistor (TFT), and each color filter only transmits the designated color. Finally, a full-color image is generated. In our simulation, we model the light propagation from mLED backlight to LCD panel on the basis of PSF theory [96]. Without losing generality, we assume all the mLED chips are in square shape and have the same Lambertian angular emission pattern. For simplicity, we used Gaussian spatial distribution and Lambertian angular profile to describe the output light from diffuser. In order to validate our model, we compared our simulation results with the experimental data reported in [93]. On the four investigated test patterns, the dynamic contrast ratio values agree reasonably well except for variations at detector noise level [21].

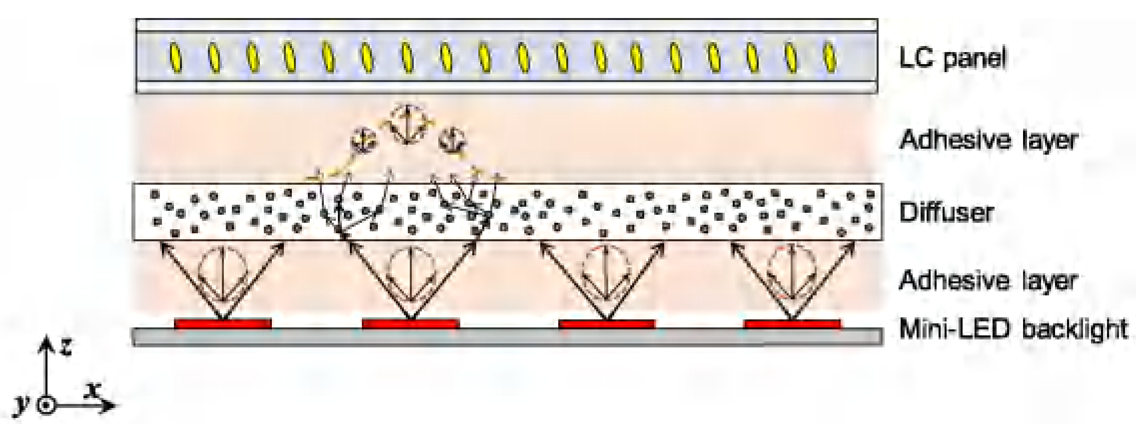

Figure 5-2 Schematic diagram of mini-LED backlit LCD.

5.2.2 Display performance evaluation metric

After validating the simulation model, we further investigate in the relationship between device structure and the final HDR display performance, especially the halo effect and clipping effect. The light modulation process is illustrated in Figure 5-3, where the displayed image is a candle. Here, the backlight consists of 12×24 local dimming zones and each zone contains 6×6 mLEDs in order to achieve a desired luminance. According to the image content, the mLEDs in each dimming zone are pre-determined to show different gray levels, as Figure 5-3(a) depicts. After passing through the diffuser, the outgoing light spreads out in each local dimming zone before reaching the LC panel [Figure 5-3(b)]. And the LC panel generates a full-color image as Figure 5-3(c) show.

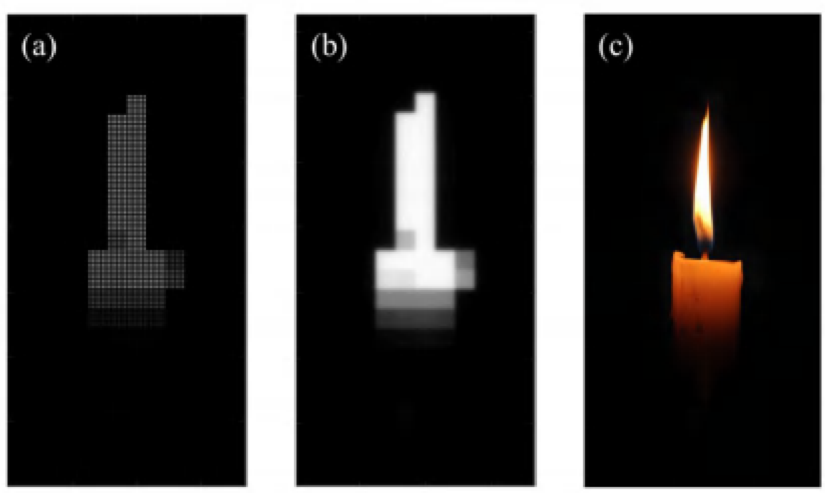

Figure 5-3 Light modulation of mLED-LCD: (a) mLED backlight modulation; (b) luminance distribution of the light incident on the LC layer, and (c) displayed image after LC panel modulation.

In order to quantitatively measure halo effect and clipping effect, we adopt peak signal-to-noise ratio (PSNR) in the CIE 1976 $L^*a^*b^*$ color space as our evaluation metric [96]:

$$LabPSNR = 10 \times \log_{10}\left[\frac{(\Delta E_{\max})^2}{\frac{1}{mn}\sum_{i=1}^{n}\sum_{j=1}^{m}\Delta E(i,j)^2}\right]. \quad \textbf{(5-1)}$$

In Equation (5-1), $\Delta E_{\max}$ is the color difference between black and white ($\Delta E_{\max}$ = 100 in our simulation); ΔE (i, j) is the color difference between the displayed image and the target image on the pixel (i, j); m and n are the image resolution (2880×1440 in our example). The color difference is defined in $L^*a^*b^*$ color space considering luminance and chrominance differences:

$$\Delta E = \sqrt{\Delta L^{*2} + \Delta a^{*2} + \Delta b^{*2}}. \quad \textbf{(5-2)}$$

From definition, higher *LabPSNR* implies better image reproduction. We will use this evaluation metric for further discussions.

5.2.3 Perception limit

Local dimming LCD may never reproduce exactly the same image content as emissive displays with pixel-level dimming and intrinsic high contrast ratio. Whereas, it is able to provide the comparable viewing experience to customers if the difference so small that it exceeds the perception limit of human eyes. In order to find the perception limit of noticing halo effect and clipping effect, we designed and conducted the following subjective experiments.

We evaluated ten HDR image contents with dark area and highlight spots, and seventy mLED-LCD system configurations: ten local dimming zone numbers and seven LC CRs. For each content and each rendering condition, we simulated the displayed image and calculated the corresponding *LabPSNR* taking the original target image as the reference. Eleven people with normal or corrected normal vision (average age = 25.5) independently participated in the experiment in a darkroom. In each test, a simulated mLED-LCD displayed image and the corresponding target image were displayed on two OLED smartphones (peak luminance = 1000 cd/m^2). Each observer was asked to compare the two images at 25-cm viewing distance and select the one they preferred. The location of the two images were randomly shifted to avoid the influence of prejudgment and viewing angle. In total, we conducted 770 tests (70 rendering conditions × 11 observers) and summarized the results in Figure 5-4.

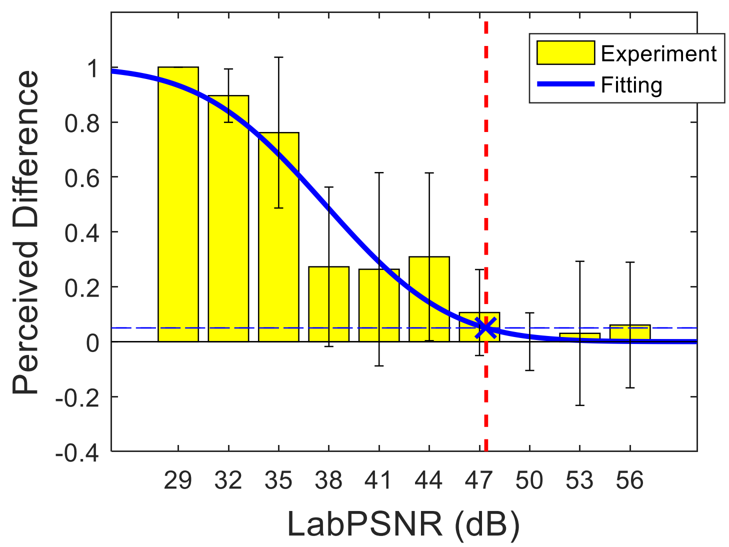

Figure 5-4 Subjective experiment results of perceived image difference versus LabPSNR of the images.

In Figure 5-4, the perceived difference stands for the ratio of observers who are able to distinguish the target images from the simulated displayed images by the mLED-LCD system. The *LabPSNR* values of the 70 rendered images scatter over a wide range from 28 dB to 57 dB. The yellow bar denotes the averaged perceived difference ratio in each *LabPSNR* range, and the black error bar marks the standard deviation of the experimental data. The blue solid line is fitted with cumulative distribution function [21,97]. Here, it delineates the probability that people can perceive the difference at a given image pair with *LabPSNR*. The good match between fitting curve and experimental data delivers the first message: *LabPSNR* could be used to predict the human perceptibility of the displayed images. The second message can be found from the blue cross in Figure 5-4, for a displayed image with *LabPSNR* > 47.4 dB, only less than 5% of people could perceive the difference between the displayed image and target image, indicating an effective suppression of halo effect and clipping effect. In the following discussions, we will use *LabPSNR* > 47.4 dB as our optimization target.

5.3 Optimization strategies

5.3.1 Local dimming zone number and LC contrast ratio

Mini-LED backlight unit can suppress halo effect and clipping effect by properly choosing LC CR and local dimming zone density [30]. Through simulations, we found the correlation between the LC CR, local dimming zone number and *LabPSNR*, as plotted in Figure 5-5. In Figure 5-5, the black dashed lines mark the criterion *LabPSNR* = 47.4 dB, above which the halo effect and clipping effect are unnoticeable for > 95% people. High *LabPSNR* can be acquired by increasing the number of local dimming zones and by increasing the LC CR. If the LC CR is 1000:1, e.g. the CR of a twisted nematic (TN) LC panel, then even 10 000 zones are still inadequate. However, for a fringing-field switching (FFS) LC panel with CR = 2000:1, *LabPSNR* > 47.4 dB can be acquired with ~ 3000 local dimming zones. Moreover, when a multi-domain vertical alignment (MVA) LC panel with CR = 5000:1 is employed, that criterion can be met with ~ 200 zones. Larger number of local dimming zones can further reduce the perceptibility on the less than

5% people, but the tradeoff is a higher panel cost. To be noticed, these results are based on a 6.4-inch smartphone placed at 25-cm viewing distance. They can be scaled up and applied to large-size panels as well [21].

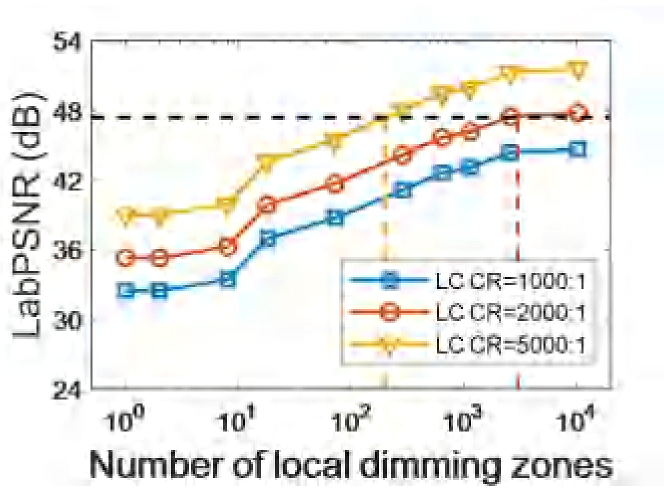

Figure 5-5 Simulated LabPSNR for HDR display systems with various local dimming zone numbers and contrast ratio.

5.3.2 LED light expansion and local light confinement

The number of local dimming zones and LC CR have the dominant impacts on local dimming effect. However, between two comparable panels (similar LC CR, panel size and viewing distance), sometimes the one with fewer local dimming zones could exhibit a better performance, which is contradictory to the general trend shown in Figure 5-5. This conflict comes from the different optical designs, where LED light expansion and local light confinement also jointly contribute to the final local dimming performance. In the following, we will discuss the influence of each factor and then suggest the corresponding optimization strategies.

From mLED backlight to LC layer, the light profile of each LED could expand from the original square-shaped Lambertian distribution to a Gaussian-like spatial and Lambertian-angular profile. The final profile is influenced by several factors including the LED emission aperture, the distance between mLEDs and diffuser, and other optical layers such as brightness enhancement film, dual brightness enhancement film, etc. Figure 5-6 depicts an exemplary one-dimensional light profile. Here, we assume six mLEDs (N_{LED} = 6) locate at x_{LED} = ±0.5, ±1.5, and ±2.5, with an interval Δx_{LED} = 1. In reality, there are 6×6 mLEDs in the central dimming zone. They are turned-on together, while the adjacent zones are dimmed to the dark state. In Figure 5-6, each black curve depicts the light profile entering the LC layer from each individual mLED, and the blue curves delineate the single-zone light profile. Because the light experiences propagation and diffusion before entering the LC layer, here we use Gaussian function to fit the expanded single-LED light profile:

$$I(x_{LED}) \propto \exp\left[-\frac{(x_{LED}-x_{LED\_c})^2}{2\sigma^2}\right], \tag{5-3}$$

where x_{LED_c} is the locus of the source LED and σ is an expansion characteristic parameter.

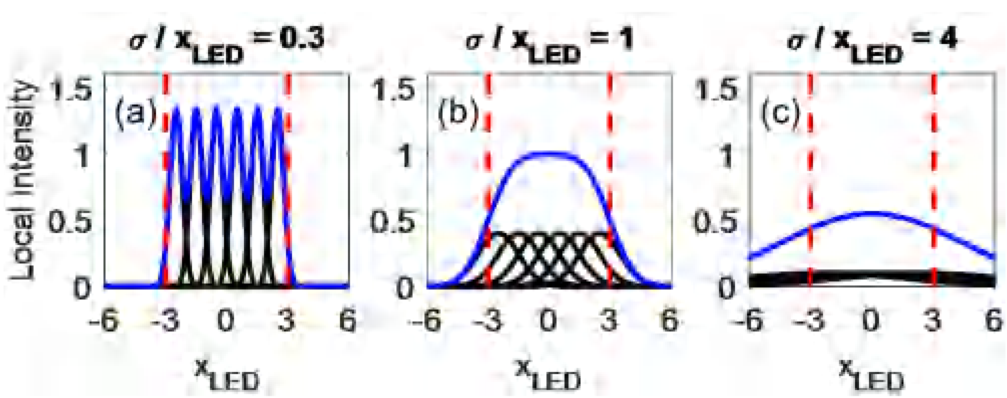

Figure 5-6 Simulated spatial profiles of local dimming BLUs with different σ / x_{LED} values.

In Figure 5-6, the vertical red dashed lines denote the local dimming zone borders. As we can see, a small σ / x_{LED} helps confine the light in the local area [Figure 5-6(a)] while more than one-half of the light energy would spread outside the zone when σ / x_{LED} is large [Figure 5-6(c)].

Such a crosstalk could impair the local dimming function and give rise to the unwanted halo effect and clipping effect.

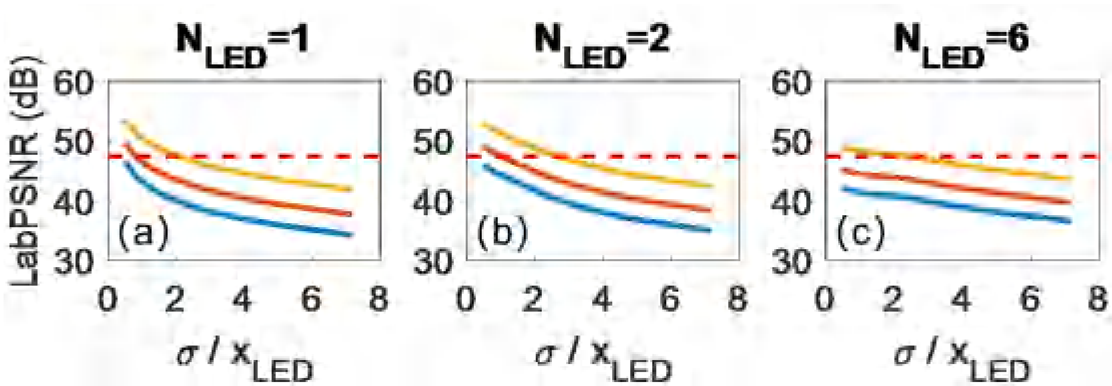

Figure 5-7 Simulated LabPSNR for HDR display systems. The blue, red and yellow lines stand for CR = 1000:1, 2000:1 and 5000:1, respectively.

Figure 5-7 shows that for a given number of LEDs in a local dimming zone (N_{LED}), better image fidelity (higher *LabPSNR*) can be obtained by a smaller σ / x_{LED}, corresponding to a smaller LED emission aperture and shorter optical distance. The latter leads to a thinner panel profile. However, the associated challenges are thermal management, manufacturing yield, and especially the compromised luminous uniformity. Figure 5-6(a) shows that if the LED light does not spread wide enough, the resultant backlight intensity could be very sensitive to the spatial location. Therefore, a proper σ / x_{LED} should be selected. For instance, $\sigma / x_{LED} = 0.5$ could provide > 97% backlight uniformity, which enables unnoticeable halo effect and clipping on a local dimming LCD with 2×2 LEDs per local dimming zone and CR = 2000:1 [Figure 5-7(b)]. In Figure 5-7, if we compare the *LabPSNR* values at $\sigma / x_{LED} = 0.5$ and an identical CR, we find that a smaller N_{LED} leads to a higher *LabPSNR*. The reason is that here we use the same LED dimension parameters and panel size for simulation. In other words, the smaller N_{LED}, the larger number of local dimming zones, therefore the higher *LabPSNR*. In a mLED backlit LCD system, σ / x_{LED} can be obtained by Gaussian fitting the expanded spatial luminous profile of each mLED.

To reduce crosstalk between adjacent local dimming zones without compromising uniformity, optical structures such as bank isolation [98] or lens collimation [99] can be employed at zone level. Ideally, a rectangular light profile can generate uniform local dimming backlight without crosstalk. Whereas, in practical designs only flattop profile can be realized, which can be described by a super-Gaussian function as:

$$I(x_{zone}) \propto \exp\left[-\left|\frac{x_{zone}-x_{zone\_c}}{\sqrt{2}\sigma}\right|^{\beta}\right]. \qquad \textbf{(5-4)}$$

Similar to above discussion, here we assume the center of the local dimming zones (x_{zone_c}) are x_{zone} = 0, ±1, ±2, … with interval Δx_{zone} = 1. In Figure 5-8, each black curve depicts a spatial profile of light generated by the zone under its curve center, while the red dashed lines delineate the borders of the zone at x_{zone_c} = 0. We set σ / x_{zone} ~ 0.5 in order to obtain good overall uniformity, as the blue curves indicate. Figure 5-8 shows that as β increases from 2 to 25, the crosstalk is reduced so that the clipping effect is lessened accordingly. Although the uniformity is improved noticeably from Figure 5-8(a) to Figure 5-8(c), at large β [Figure 5-8(c)] we found abrupt luminance change at zone borders. If the compensation at borders is not performed carefully, the incongruous lines could be noticeable in the actual display panel. In practical manufacturing, this issue can be aggravated by uneven distribution of local dimming zone and the misalignment between local dimming zone and compensation.

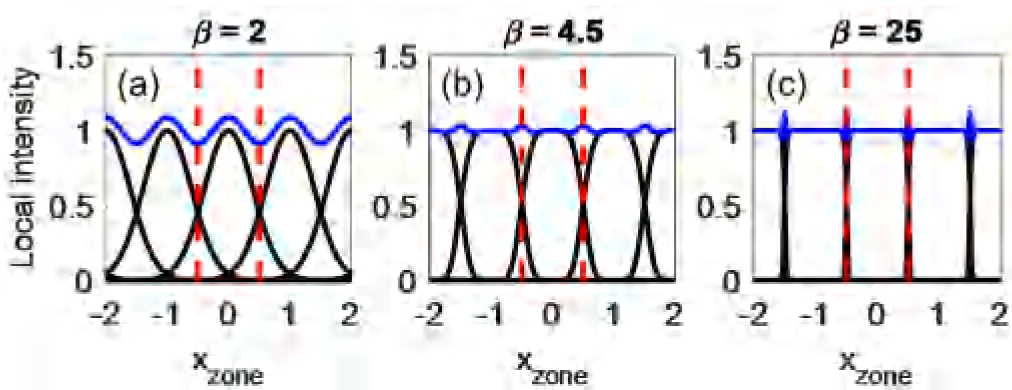

Figure 5-8 Simulated spatial profiles of different local dimming BLU with different β.

Figure 5-9 demonstrates that good light confinement (high β) helps improve image quality. As β increases, *LabPSNR* increases initially but saturates as β exceeds 4.5. This implies local light confinement is helpful to certain degree. In contrast, high LC CR and short zone pitch (p_{zone}) help enhance the *LabPSNR* value more obviously. When $\beta > 2$, an unnoticeable halo effect and clipping effect can be achieved for the LC panels with CR > 1000:1 (blue lines), 2000:1 (red lines) and 5000:1 (yellow lines) with p_{zone} = 1 mm [Figure 5-9(a)], 2 mm [Figure 5-9(b)] and 6 mm [Figure 5-9(c)], respectively. In practice, β can be extracted from a mLED enhanced LCD by super-Gaussian fitting the spatial luminous profile of single-lit local dimming zone.

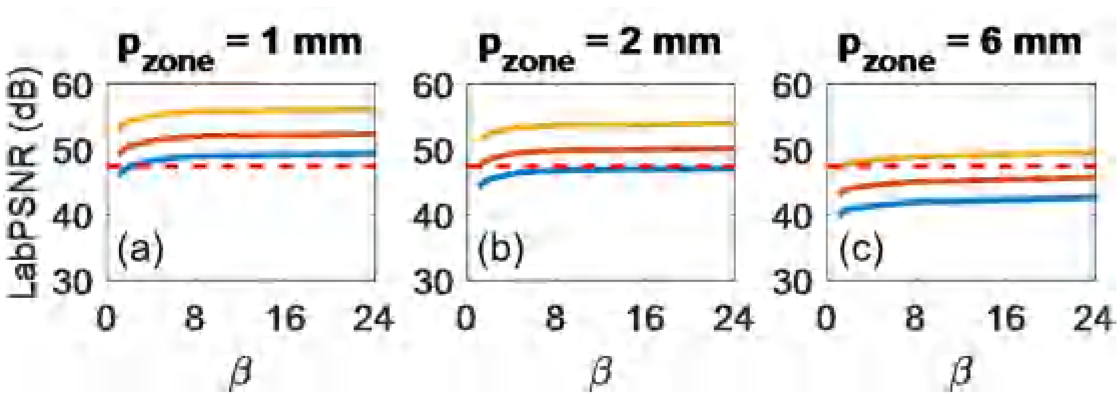

Figure 5-9 Simulated LabPSNR for HDR display systems with various p_{zone}. The blue, red and yellow lines stand for LC CR=1000:1, 2000:1 and 5000:1, respectively.

5.4 Conclusion

In this chapter, we developed a simplified model for optimizing high contrast ratio mLED-LCD system. Through numerical simulation and subjective experiments, we find that the halo effect and clipping effect in local dimming LCD can be suppressed to an unnoticeable level by increasing LC CR and local dimming zone number. Specifically, we found that for a 6.4-inch smartphone at 25-cm distance, around 3000 and 200 local dimming zones are required for an FFS LCD with CR = 2000:1 and an MVA LCD panel with CR = 5000:1, respectively. These results can be extended to large-size panels according to the viewing distance. Besides, confining light in each local dimming zone can reduce inter-zone crosstalk, which alleviates halo effect and clipping effect from the root. We found that it is beneficial to have flattop spatial light profile for each local dimming zone, which significantly improves display fidelity from the Gaussian distribution generated from thick diffuser, and that is less vulnerable to backlight uniformity and misalignment tolerance issues than square-shaped profile. This work paves the way for achieving HDR performance in mLED-LCDs.

CHAPTER 6 HIGH POWER EFFICIENCY

6.1 Introduction

Absolute high peak luminance is indispensable in high dynamic range displays, not only for faithfully reproducing highlight image contents, but also for enhancing ambient contrast ratio. Whereas, in systems with limited output power efficiency, high luminance can cause short battery time and thermal management issues. In non-emissive LCDs, though high luminance can be boosted by the inorganic LED backlight, the optical efficiency is relatively low (~ 5%). Emissive displays have much higher optical efficiency (40% ~ 90%), but the overall power efficiency does not increase proportionally. In OLED emissive displays, that results from the lower external quantum efficiency (EQE) of OLED chips than inorganic LEDs. Even worse is that organic materials are vulnerable to fast aging [14] and efficiency roll-off [15] at high luminance. Inorganic LED materials are inherently robust. Hence, high luminance does not impair the lifetime of inorganic mLED/μLED displays. However, the EQE of inorganic mLED/μLED chips is very sensitive to chip size and current density [20,31,32]. If improperly operated, most of the energy will be consumed by non-radiative recombination, resulting in low power efficiency. Specifically, the EQE of LED chip (EQE_{chip}) is the product of LED internal quantum efficiency (IQE) and light extraction efficiency. Figure 6-1(a) depicts the current density dependent IQE of blue inorganic LEDs with various chip size (data from [31,32]). In physics, Shockley-Read-Hall non-radiative recombination and Auger non-radiative recombination respectively impair the IQE of inorganic LED chips at low current density and high current density [31]. Consequently, the peak of EQE_{chip} locates at moderate current density. Small chips have higher surface-to-volume ratio so that

Shockley-Read-Hall non-radiative recombination is aggravated. Correspondingly, we can see small chips have lower IQE in the low current density region in Figure 6-1(a). Besides, although high EQE_{chip} has been achieved on large chips (e.g. > 80% on blue), µLEDs (s < 50 µm) endure insufficient light extraction [100]. The state-of-the-art peak EQE_{chip} of R/G/B (red/green/blue) mLED/µLED chips is summarized in Figure 6-1(b) [20,101,102], as denoted by R/G/B line colors, respectively. We can see that small chip size could harm the peak EQE_{chip} on R/G/B inorganic LEDs.

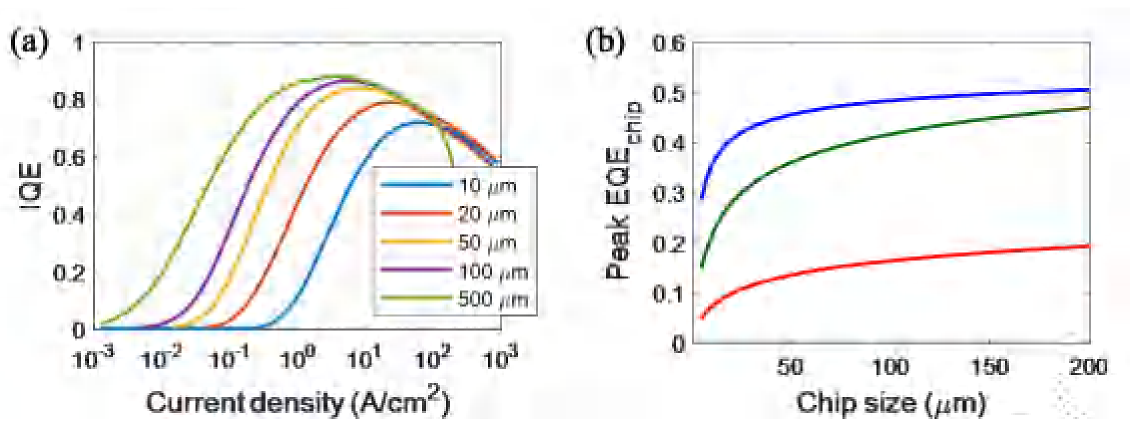

Figure 6-1 (a) Current density dependent internal quantum efficiency (IQE) for different mLED/µLED chip size. (b) Chip size dependent peak EQE_{chip} of R/G/B mLED/µLED chips, represented by R/G/B line colors, respectively.

In order to develop high-luminance mLED/µLED displays with high power efficiency, in this chapter, we build a power efficiency model for mLED/µLED displays. Our study starts from LED physics and integrates the factors of display optical systems. We apply the model to RGB-chip emissive displays, color conversion emissive displays and mLED-LCDs, and find the model in good agreement with experimental measurements. Our model provides a power consumption evaluation method from physics, and reveals that proper system configuration, small emission aperture ratio and pulse width modulation are critical methods to enhance the power efficiency of mLED/μLED displays.

6.2 Power efficiency model

6.2.1 Monochrome LED power efficacy

The analysis starts from the input electrical power (P_{LED} [unit: W]) of a mLED/μLED:

$$P_{LED} = V_F \cdot I, \tag{6-1}$$

where I is the current through LED, and V_F is the LED forward voltage. The output optical power (P_{op} [unit: W]) is:

$$P_{op} = \frac{I}{e} \cdot EQE_{chip} \cdot E_{ph}. \tag{6-2}$$

Here e and E_{ph} stand for elementary charge and photon energy, respectively. The luminous flux emitted from the LED (Φ [unit: lm]) is related to P_{op} and luminous efficacy (K [unit: lm/W]) as:

$$\Phi = K \cdot P_{op}, \tag{6-3}$$

$$K = \frac{\int V(\lambda) S(\lambda) d\lambda}{\int S(\lambda) d\lambda}, \tag{6-4}$$

where $V(\lambda)$ is the spectral luminous efficacy and $S(\lambda)$ is the LED emission spectrum. From above equations, the LED power efficacy (η_{LED} [unit: lm/W]) can be expressed as:

$$\eta_{LED} = \frac{\Phi}{P_{LED}} = \frac{K \cdot E_{ph}}{e} \cdot \frac{EQE_{chip}}{V_F}. \tag{6-5}$$

6.2.2 Full-color device power efficacy

Next, we would consider the device structure beyond LED chip. Assuming the system optical efficiency as T_{sys}, the on-axis panel luminance (L [unit: cd/m^2]) for j = R, G, B colors is

$$L_j = \frac{\Phi_j \cdot T_{sys,j}}{p^2 \cdot F_j}. \tag{6-6}$$

Here, p is the pixel pitch and F [unit: sr] is the conversion coefficient from on-axis luminous intensity [unit: cd] to luminous flux Φ [unit: lm]:

$$F_j = \iint f_j(\theta, \varphi) \cdot \sin\theta \cdot d\theta \cdot d\varphi, \tag{6-7}$$

where $f(\theta, \varphi)$ is the angular profile of display intensity as a function of polar angle θ and azimuthal angle φ. Correspondingly, the on-axis luminous power efficacy (η [unit: cd/W]) is

$$\eta_j = \frac{L_j}{P_{LED,j} / p^2} = \frac{K_j \cdot E_{ph,j}}{e} \cdot \frac{EQE_{chip,j} \cdot T_{sys,j}}{V_{F,j} \cdot F_j}. \tag{6-8}$$

In full-color displays, in order to obtain D65 white light (luminance L_W), the monochromatic luminance L_j is mixed by

$$L = \begin{bmatrix} L_R \\ L_G \\ L_B \end{bmatrix} = L_W \cdot \begin{bmatrix} r_R \\ r_G \\ r_B \end{bmatrix}, \tag{6-9}$$

where the color mixing ratio r_j satisfies

$$r_R + r_G + r_B = 1. \tag{6-10}$$

From Equation (6-8), the on-axis luminous power efficacy for mixed white light is

$$\eta_W = \frac{L_W}{P_{LED,W} / p^2} = \frac{L_W}{\sum_{j=R,G,B} P_{LED,j} / p^2} = \frac{L_W}{\sum_{j=R,G,B} \frac{L_j}{\eta_j}} = \frac{1}{\sum_{j=R,G,B} \frac{r_j}{\eta_j}}. \tag{6-11}$$

In the following discussion, we use Equation (6-11) to evaluate the η_W of mLED/μLED displays with different system configurations.

6.2.3 RGB-chip emissive displays

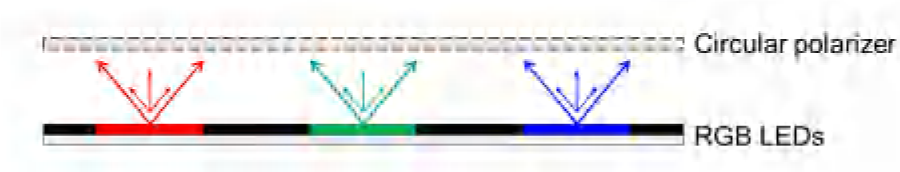

Figure 6-2 Optical structure of a RGB-chip mLED/μLED emissive display.

Figure 6-2 illustrates the optical structure of a RGB-chip mLED/μLED emissive display. In this type, R/G/B mLED/μLED chips are adopted and each chip serves as a subpixel. The light is emitted upward and downward from LEDs. In order to reflect the downward light upward, a reflective electrode is commonly deposited at the bottom of each LED chip. Whereas, such a reflector also reflects the incident ambient light, which could degrade the ambient contrast ratio. In order to enhance ambient contrast ratio, a circular polarizer (CP) is optionally laminated above LEDs. In some CP-free configurations, tiny LED chips are adopted to reduce the aperture ratio, and the non-emitting area is covered by black matrix so that most of the ambient light is absorbed. This small-aperture strategy is unique for inorganic LEDs. In comparison, large chip size is needed for OLED displays in order to achieve long lifetime and high luminance so that a CP is necessary [33]. In CP-laminated designs, T_{sys} equals to T_{CP} = 42%. For RGB-chip emissive mLED/μLED displays, F is determined by the LED's angular emission profile, which is close to Lambertian (F = π sr). The mLED/μLED sidewall emission increases the ratio of light emitted to large angles, leading to a larger F and lowers the ratio of light contributing to on-axis intensity. This phenomenon is more severe on the smaller-size μLEDs [100]. For RGB-chip emissive displays, the on-axis luminous power efficacy is:

$$\eta_{RGB,j} = \frac{K_j \cdot E_{ph.j}}{e} \cdot \frac{EQE_{chip,j} \cdot T_{CP,j}}{V_{F,j} \cdot F_j}. \qquad \textbf{(6-12)}$$

Table 6-1 On-axis power efficacy of a RGB-chip mLED emissive display.

Color	Red	Green	Blue
K (lm/W)	260	652	77
E_{ph} (J)	3.2×10^{-19}	3.7×10^{-19}	4.2×10^{-19}
EQE_{chip}	0.11	0.31	0.45
V_F (V)	1.72	2.33	2.49
F (lm/cd)	4.67	3.67	3.67
T_{CP}	0.42		
r	0.270	0.616	0.114
η_{RGB} (cd/W)	2.9	22.9	4.2
P / P_W	0.63	0.18	0.19
$\eta_{RGB,W}$ (cd/W)	6.8		

Table 6-1 is an exemplary calculation for a RGB-chip mLED emissive display. We used the data of R/G/B mLED chips (dimension = 90 μm × 130 μm) operated at I = 50 μA, and found $\eta_{RGB,W}$ as 6.8 cd/W. From Table 6-1 we can see, because of the relatively low $EQE_{chip,R}$, the red chip consumes more than half of the power. Technology innovation to improve $EQE_{chip,R}$ of mLED is urgently needed. Figure 6-3 depicts the simulated chip size dependent η_{RGB} with data in Figure 6-1(b). The R/G/B and black lines stand for the simulated values for R/G/B and white light, respectively. We can see green light has a higher η_{RGB} than the red/blue, which results from the larger K_G – higher human eye responsivity. The left axis and the right axis in Figure 6-3 are for devices without and with a circular polarizer, respectively. The difference between the two axes is T_{CP}. For large-aperture RGB-chip emissive displays, the CP lamination will cut the optical efficiency by more than a half, resulting in relatively low η_{RGB}.

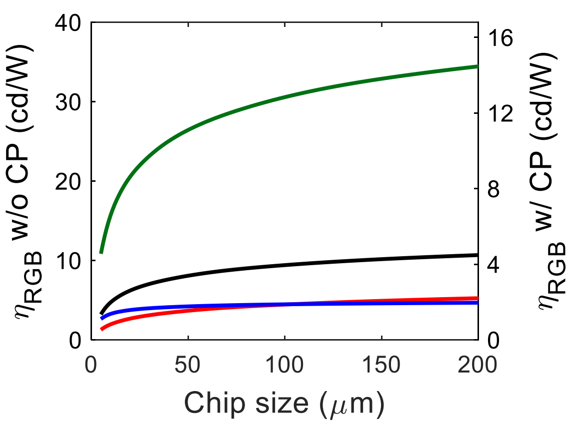

Figure 6-3 Chip size dependent on-axis luminous power efficacy of a RGB-chip mLED/μLED emissive display. The R/G/B and black lines stand for the simulated values for R/G/B and white light, respectively. The left axis and the right axis are for optical structures without and with circular polarizer, respectively.

6.2.4 Color conversion emissive displays

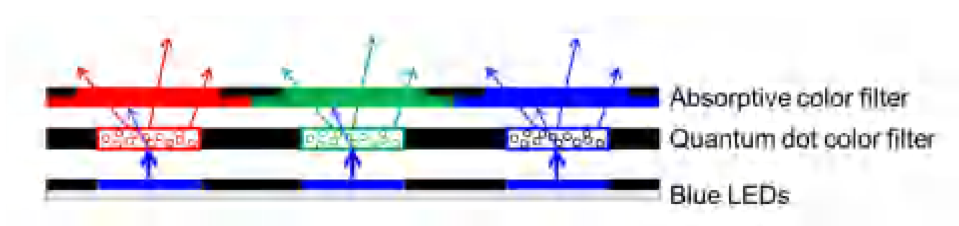

Figure 6-4 Optical structure of a color conversion mLED/μLED emissive display.

Figure 6-4 illustrates the optical structure of a color conversion mLED/μLED emissive display. In this type, each blue LED chip pumps a subpixel in the registered color conversion layer so that it bypasses the need of high-EQE_{chip} red mLEDs/μLEDs. In Figure 6-4, color conversion is realized by a quantum dot color filter (QDCF) [103]. The overall EQE for each subpixel becomes a product of blue chip EQE ($EQE_{chip,B}$) and QDCF's color conversion efficiency (EQE_{QDCF}). Here, EQE_{QDCF} is jointly determined by the film's quantum yield and the light extraction efficiency. In color conversion emissive displays, the image quality may be degraded for two reasons: 1) The unconverted blue light may leak out from red and green subpixels; 2) the shortwave component in ambient light may excite the QDs. In order to absorb the unconverted blue light and to suppress ambient excitation, an absorptive color filter is above registered, which can be presented by its transmittance (T_{CF}). It also alleviates ambient light reflection so that no circular polarizer is needed. In some designs, a distributed Bragg reflector (DBR) is inserted to selectively recycle the unconverted blue light [104] or to enhance the red and green output efficiency [105]. For color conversion emissive mLED/μLED displays, F is determined by the angular profile of the light output color conversion layer and absorptive color filter, which is also close to Lambertian ($F = \pi$ sr). For color conversion emissive displays, the on-axis luminous power efficacy is:

$$\eta_{CC,j} = \frac{K_j \cdot E_{ph.j}}{e} \cdot \frac{EQE_{chip,B} \cdot EQE_{QDCF,j} \cdot T_{CF,j}}{V_{F,B} \cdot F_j}. \quad \textbf{(6-13)}$$

Table 6-2 is an exemplary calculation for a color conversion mLED/μLED emissive display. Using the same blue mLED that adopted in Table 6-1, $\eta_{CC,W}$ of a color conversion mLED emissive displays is 12.0 cd/W. Figure 6-5 depicts the simulated chip size dependent η_{CC} with data in Figure 6-1(b). Similar to Figure 6-3, the R/G/B and black lines stand for the simulated values for R/G/B and white light, respectively. In above calculations, we used EQE_{QDCF} = 0.3~0.38 as reported by Nanosys [103]. As EQE_{QDCF} being improved, the color conversion type can be more power saving.

Table 6-2 On-axis power efficacy of a color conversion mLED emissive display.

Color	Red	Green	Blue
K (lm/W)	207	561	77
E_{ph} (J)	3.2×10^{-19}	3.7×10^{-19}	4.2×10^{-19}
EQE_{chip}	-	-	0.45
V_F (V)	-	-	2.49
EQE_{QDCF}	0.38	0.30	0.9
$EQE_{chip,B} \cdot EQE_{QDCF}$	0.17	0.13	0.41
F (lm/cd)	3.14	3.14	3.14
T_{CF}	0.82	0.91	0.72
r	0.293	0.594	0.113
η_{CC} (cd/W)	7.4	20.6	7.5
P / P_W	0.47	0.35	0.18
$\eta_{CC,W}$ (cd/W)	12.0		

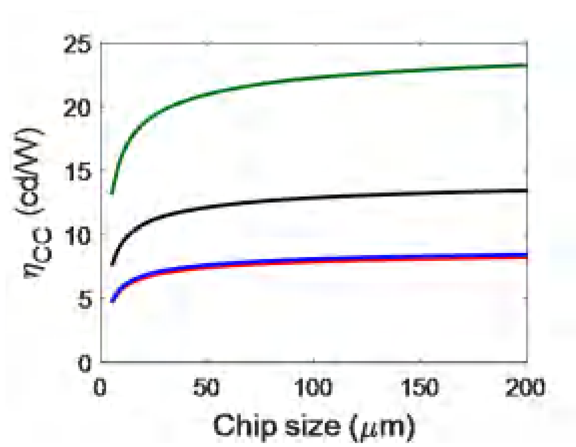

Figure 6-5 Chip size dependent on-axis luminous power efficacy of a color conversion mLED/µLED emissive display. The R/G/B and black lines stand for the simulated values for R/G/B and white light, respectively.

6.2.5 Mini-LED backlit LCDs

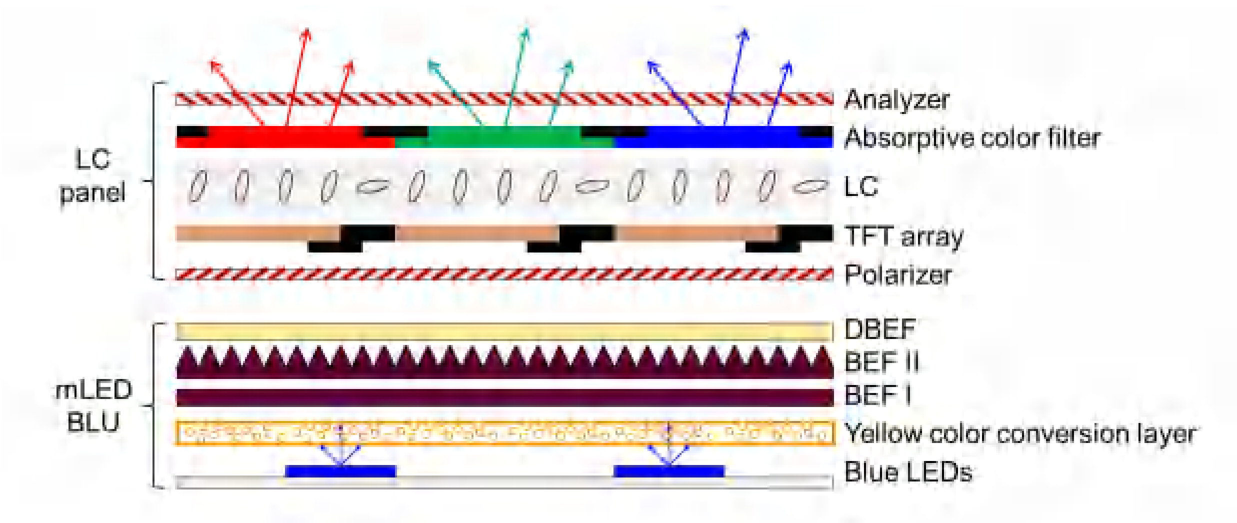

Figure 6-6 Optical structure of a mLED backlit LCD with a RGB absorptive color filter.

As illustrated in Figure 6-6, a mLED-LCD is to substitute the traditional backlight of LCD with a local dimming mLED backlight unit (BLU). In such a BLU, the mLEDs do not need to register with the subpixels in LC panel so that larger LED chips can be used. The main power consumption of mLED-LCD originates from the BLU. In Figure 6-6, the blue LED light is converted to white through a yellow color conversion film with efficiency EQE_{QDEF} (≈ 0.73 from 3M quantum dot enhancement film). Similar to color conversion emissive displays, mLED BLU can optionally adopt a DBR. Because the color conversion layer scatters light, up to two brightness enhancement films (BEFs) can be employed to collimate light onto on-axis direction. A dual brightness enhancement film (DBEF) can be inserted to transmit the preferred polarization, which is parallel to the transmission axis of the first polarizer in LC panel, and to recycle the orthogonal polarization. As an example, F can be reduced to 0.96 sr by applying two BEFs and one DBEF (3M Vikuiti™). These optical films correspond to a luminous transmission T_{BLU} (≈ 0.9). Then the light is modulated by a LC panel with an absorptive RGB color filter array whose optical efficiency is T_{LCD} (≈ 5%). For mLED-LCDs, the on-axis luminous power efficacy is:

$$\eta_{LCD,j} = \frac{K_j \cdot E_{ph.j}}{e} \cdot \frac{EQE_{chip,B} \cdot EQE_{QDEF,j} \cdot T_{BLU} \cdot T_{LCD}}{V_{F,B} \cdot F_j}. \tag{6-14}$$

Table 6-3 On-axis power efficacy of a mLED backlit LCD with a RGB absorptive color filter.

Color	Red	Green	Blue
K (lm/W)	186	526	84
E_{ph} (J)	3.1×10^{-19}	3.7×10^{-19}	4.3×10^{-19}
EQE_{chip}	-	-	0.5
V_F (V)	-	-	2.8
EQE_{QDEF}	0.73	0.73	1
$EQE_{chip,B} \cdot EQE_{QDEF}$	0.37	0.37	0.5
T_{BLU}	0.9		
F (lm/cd)	0.96		
T_{LCD}	0.05		
r	0.247	0.672	0.081
η_{LCD} (cd/W)	2.2	7.4	1.9
P / P_W	0.45	0.37	0.18
$\eta_{LCD,W}$ (cd/W)	4.1		

Table 6-3 is an exemplary calculation for a mLED-LCD. The simulated $\eta_{LCD,W}$ is 4.1 cd/W. For a 65-inch 4K-resolution TV with 1000-cd/m^2 peak luminance, the corresponding power consumption is $P_{LED,W}$ = 284 W, which agrees very well with the measured 280 W. Figure 6-7 depicts the simulated chip size dependent η_{LCD} with data in Figure 6-1(b). Similar to Figure 6-3 and Figure 6-5, the R/G/B and black lines stand for the simulated values for R/G/B and white light, respectively. To be noticed, in emissive displays, the chip size should be smaller than the pixel pitch. But larger-size LEDs can be used in mLED BLU, enabling higher EQE_{chip}. In some designs, a RGBW color filter is employed, corresponding to a higher T_{LCD} (≈ 10%) and a doubled η_{LCD}.

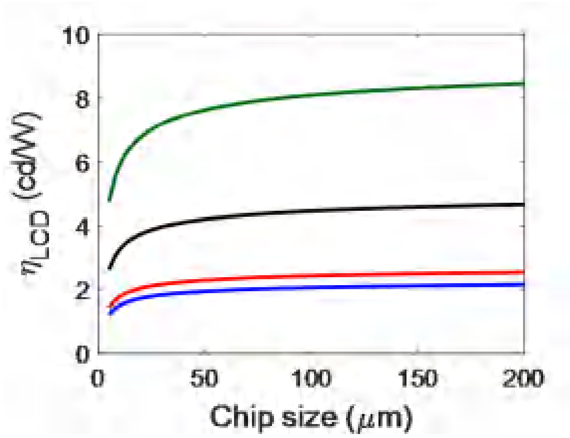

Figure 6-7 Chip size dependent on-axis luminous power efficacy of a mLED backlit LCD with a RGB absorptive color filter. The R/G/B and black lines stand for the simulated values for R/G/B and white light, respectively.

6.3 Enhancement strategies

6.3.1 Proper system configuration

System configuration predetermines the power efficacy. Figure 6-8 summarizes the chip-size dependent on-axis luminous power efficacy of the abovementioned system configurations. As a reference, we added a RGB-chip OLED emissive display in Figure 6-8, as shown by the black dashed lines, whose EQE_{chip} does not vary drastically with chip size and operation current density. Here, state-of-the-art OLED chips [106-109] are used in evaluation, whose EQE_{chip} for [R, G, B] chip is [0.27, 0.24, 0.10]. In Figure 6-8, we can see that the mLED-LCD with a RGB color filter has a comparable η_W with the RGB-chip OLED emissive display. When s = 100 ~ 200 μm, CP-free (as delineated by the blue line) and CP-laminated (as the red line depicts) RGB-chip mLED emissive displays respectively show ~ 5× and ~ 2× higher η_W than mLED-LCD and the OLED display; while the η_W of the color conversion mLED emissive display (as shown by the yellow line in Figure 6-8) is ~ 2.5× higher. When s < 50 μm, η_W decreases noticeable as the chip size shrinks. From the on-axis power efficacy viewpoint, we received the following system configuration preference order: 1) CP-free RGB-chip mLED/μLED emissive display, 2) color conversion mLED/μLED emissive display, 3) CP-laminated RGB-chip mLED/μLED emissive display, 4) mLED-LCD and CP-laminated RGB-chip OLED emissive display.

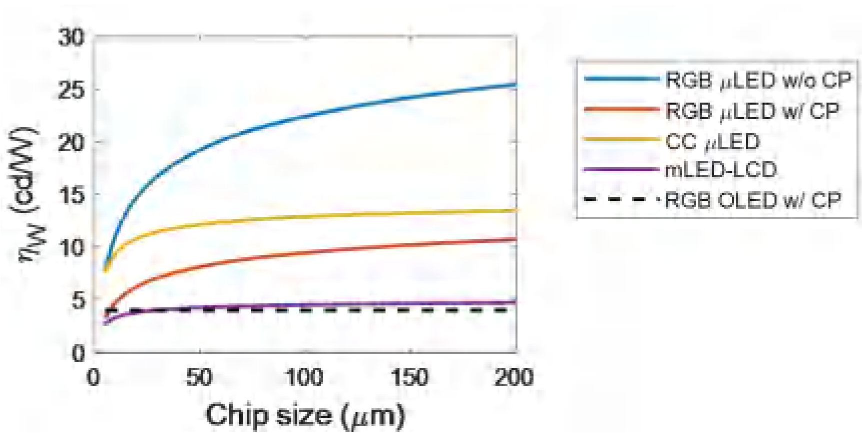

Figure 6-8 Chip size dependent on-axis luminous power efficacy of a CP-free and a CP-laminated RGB-chip mLED/μLED emissive display, a color conversion mLED/μLED emissive display, a mLED backlit LCD with a RGB absorptive color filter, and a CP-laminated RGB-chip OLED emissive display.

To be noticed, in simulating the η_W of mLED/μLED displays in Figure 6-8, peak EQE_{chip} data from Figure 6-1(b) are used. In practice, LEDs may be operated at lower EQE_{chip}, indicating lower η_W. From Equation (6-8), η_{LED} is proportional to EQE_{chip} / V_F so that high EQE_{chip} / V_F operation is beneficial to device power saving. Here, we use an example to show the influence of operation spot. Figure 6-9 depicts the characteristics of a set of R/G/B mLEDs with dimension 90 μm × 130 μm. The R/G/B chips are presented by R/G/B line colors. Figure 6-9(a) shows that the red chip exhibits lower EQE_{chip} than the green and blue chips. Apart from the IQE difference on R/G/B chips, the red semiconductor material (AlGaInP) has higher refractive index than the blue and green material (InGaN), leading to a lower light extraction efficiency on red chips. Figure 6-9(b) shows normalized EQE_{chip} / V_F as a function of current. The most power efficient LED working spots are at the peaks of EQE_{chip} / V_F. However, the LED luminance at these peaks is too high: 3~5 orders brighter than a normal display with 1000-cd/m^2 white luminance. In order to drive LED chips with high efficiency for normal-brightness panels, small aperture ratio and pulse width modulation (PWM) methods are highly recommended.

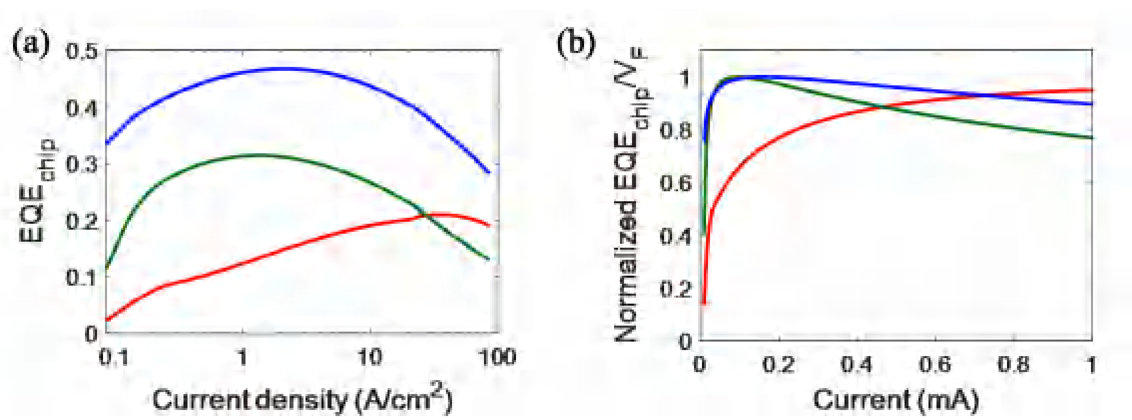

Figure 6-9 Characteristics of R/G/B mLED chips, presented by R/G/B lines, respectively. (a) EQE$_{chip}$ as a function of current density. (b) Normalized EQE$_{chip}$ / V$_F$ as a function of current.

6.3.2 Small aperture ratio

Small aperture ratio can map a high LED luminance with a low panel luminance. As drawn in Figure 6-10, the aperture ratio (AP) and LED chip size (s) are defined as:

$$AP = \frac{\text{emission area}}{\text{whole area}} = \frac{3s^2}{p^2}; \quad \textbf{(6-15)}$$

$$s = \sqrt{w \cdot l}. \quad \textbf{(6-16)}$$

Here l_1 and l_2 denote the two dimensions of LED chip, respectively. Because the panel luminance is averaged from the whole pixel, the panel luminance is AP / 3 times of the LED chip white luminance. For instance, the [R/G/B] LED chip color luminance of a panel is [30 000 cd/m^2, 60 000 cd/m^2, 10 000 cd/m^2], corresponding to 100 000-cd/m^2 white luminance. If AP = 3%, then the panel luminance is 1000 cd/m^2. By applying small aperture ratio, LED chips can be operated at 1~2 orders higher luminance than the panel.

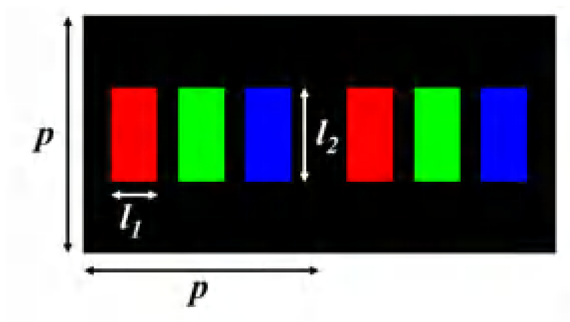

Figure 6-10 Pixel layout and dimensions of a mLED/μLED display. Each color pixel consists of three R/G/B subpixels

6.3.3 Pulse width modulation

The luminance of a display can be controlled by either pulse amplitude modulation (PAM) or pulse width modulation (PWM). PAM, also called analog driving, is to keep identity emission time in each frame, while the amplitude of electrical signal controls luminance. For a LCD, the voltage across the LC layer tunes light transmittance. For a mLED/μLED, the flowing current regulates light emittance. PWM is also denoted as digital driving, which is to switch the electrical signal between binary states (on or off at a constant signal amplitude), and to tune the luminance by adjusting the emission time in each frame. The ratio of emission time over frame time (T_f) is duty cycle (DC). As illustrated in Figure 6-11, if the instant luminous flux at on-state is Φ_{ins}, then the perceived effective luminous flux (Φ_{eff}) is

$$\Phi_{eff} = \Phi_{ins} \cdot DC. \tag{6-17}$$

The effective LED power efficacy ($\eta_{LED,eff}$) can still be calculated by Equation (6-5) since

$$\eta_{LED,eff} = \frac{\Phi_{eff}}{P_{LED,eff}} = \frac{\Phi_{ins} \cdot DC}{P_{LED,ins} \cdot DC} = \eta_{LED,ins}. \tag{6-18}$$

PWM can enhance power efficiency by the following method: Operate mLED/μLED chips at high EQE_{chip} / V_F spots. Assuming panel luminance = 10 000 cd/m^2 at DC = 100%, we can set DC = 10% for the target peak panel luminance (1000 cd/m^2). For low gray levels, adjust DC in the range of 0~10%. In this way, high efficiency is maintained at all gray levels, and the peak panel luminance is one order lower than the LED luminance. In some cases, the LED emission time at extremely low gray levels is too short for the drivers to support. In such a situation, hybrid driving may be adopted. Hybrid driving is to employ PWM at high gray levels for high efficiency and implement PAM at low gray levels for good gray level accuracy. Although the EQE_{chip} / V_F is not at the maximum when presenting low gray levels in hybrid driving, the overall power consumption remains low.

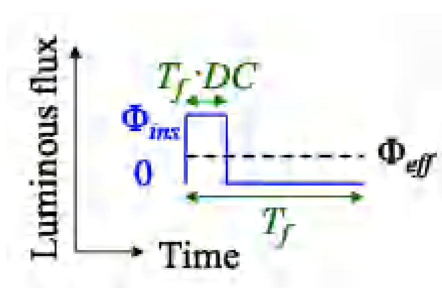

Figure 6-11 Schematic of duty cycle and effective luminance.

Depending on *DC*, the instant LED luminance can be 1~2 orders higher than the time average. In combination with small-aperture layout, additional 1~2 orders higher luminance can be attained from spatial average. In total, LEDs can be operated at around three orders higher instant luminance than the panel average. For the LEDs depicted in Figure 6-9, it means > 2× power saving.

6.4 Conclusion

In this chapter, we built a new model for simulating and optimizing the power efficiency of mLED/μLED displays. we considered the size effect of inorganic mLED/μLED chips and applied the model to different system configurations. Our simulation results show that mLED-LCD is comparable power consuming as CP-laminated RGB-chip OLED emissive displays, while color conversion mLED/μLED emissive displays, CP-free and CP-laminated RGB-chip mLED/μLED emissive displays respectively show up to 2.5×, up to 5× and up to 2× higher on-axis luminous power efficacy depending on the chip size of mLEDs/μLEDs. Moreover, based on inorganic LED characteristics, we demonstrated that small-aperture design and pulse width modulation are critical methods to achieve > 2× power saving.

CHAPTER 7 HIGH AMBIENT CONTRAST RATIO

7.1 Introduction

As discussed in Chapter 5, contrast ratio is a specification reflecting display's performance in darkroom. Nevertheless, display devices are frequently operated under ambient light. The reflected ambient light is also perceived in additional to the displayed contents. Under such a circumstance, the perceived image quality is represented by ambient contrast ratio (ACR), which is defined as follows [33]:

$$ACR = \frac{L_{on} + \frac{I_{am}}{\pi} \cdot R_L}{L_{off} + \frac{I_{am}}{\pi} \cdot R_L} \approx 1 + \frac{\pi \cdot L_{on}}{I_{am} \cdot R_L}. \tag{7-1}$$

Here, L_{on} and L_{off} (<< L_{on} for high-contrast displays) are the on- and off-state luminance of display, and I_{am} and R_L stand for the ambient illuminance and luminous reflectance of display panel, respectively. Figure 7-1 shows the simulated perceived pictures with different L_{on} and R_L under full daylight (I_{am} = 20 000 lux). The ACR is marked on the right bottom corner of each picture. From Equation (7-1) and Figure 7-1, the first method to enhance ACR is to boost L_{on} by the input power. As discussed in Chapter 6, high luminance can be managed, but high power consumption follows. The second way to improve ACR is to lower R_L, nonetheless L_{on} is also compromised in most designs. Consequently, systematic optimization is essential.

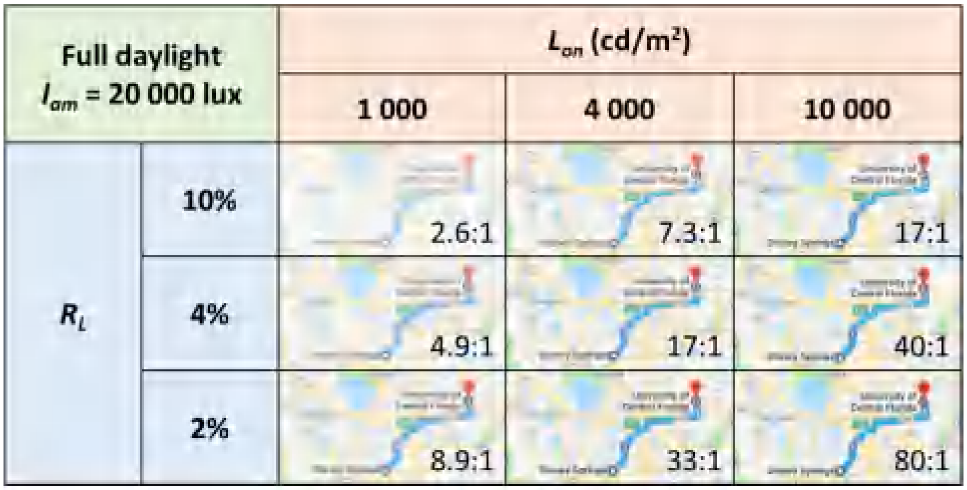

Figure 7-1 Simulated perceived images with the specified panel peak luminance and luminous reflectance under full daylight (I_{am} = 20 000 lux). The ambient contrast ratio is marked on the right bottom corner of each picture.

In this chapter we propose a figure-of-merit as a powerful tool to comprehensively optimize the power efficiency and luminous reflectance to enhance the ACR of mLED/μLED displays. Our model especially benefits RGB-chip mLED/μLED emissive displays and color conversion mLED/μLED emissive displays. It applies to various applications such as smartphones, gaming monitors and TVs. We also simulate the performance of RGB-chip OLED emissive displays and mLED-LCDs for comparison purpose.

7.2 Luminous reflectance

Figure 7-2 schematically shows the ambient reflection of mLED/μLED emissive displays. LED array and the optional optical films are encapsulated by bonding layers and a protection glass. The luminous reflectance can be described by:

$$R_L = R_s + \left(1 - R_s\right) \cdot AP \cdot R_{AP}. \tag{7-2}$$

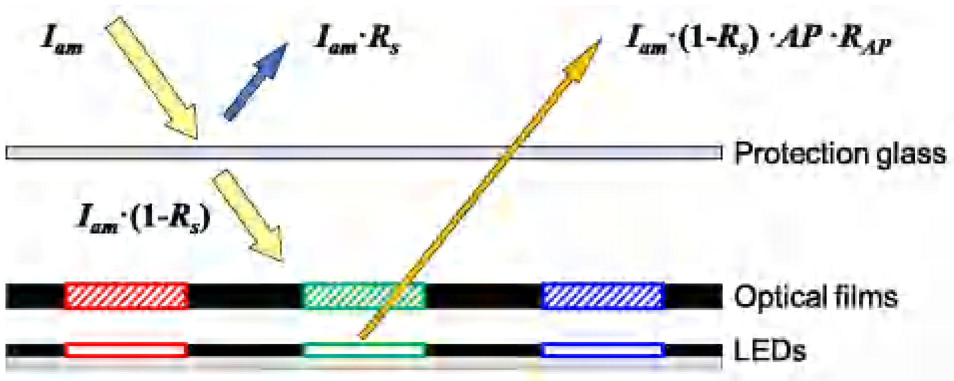

Figure 7-2 Schematic of ambient light reflection on mLED/μLED emissive display panels.

In Figure 7-2 and Equation (7-2), R_s, AP and R_{AP} stand for surface reflectance, aperture ratio and aperture luminous reflectance, respectively. Ambient reflection mainly consists of two parts: external surface reflection and internal reflection on LED electrode. First, as the blue arrow in Figure 7-2 denotes, external reflection is generated at the protection glass. Normally, R_s is ~ 4.0% for a glass-air surface, but it can be reduced to < 1.0% by sputtering anti-reflection coating on the substrates. In the following analyses, we use R_s = 2.0% for discussion purpose. Second, the internal reflection is presented by the orange arrow in Figure 7-2. As illustrated in Figure 6-10, because black matrix absorbs the transmitted ambient light [e.g. $I_{am} \cdot (1 - R_s)$], only the light that falls in the aperture is internally reflected. Accordingly, in Equation (7-2), the second term of R_L is proportional to AP. The luminous reflectance of aperture area (R_{AP}) is simulated by:

$$R_{AP} = \frac{\int_{\lambda_1}^{\lambda_2} V(\lambda)S(\lambda)R(\lambda)d\lambda}{\int_{\lambda_1}^{\lambda_2} V(\lambda)S(\lambda)d\lambda}, \tag{7-3}$$

where $V(\lambda)$ is the photopic human eye sensitivity function, as shown in Figure 7-3(a); $S(\lambda)$ is the spectrum of the ambient light (CIE Standard Illuminant D65), as plotted in Figure 7-3(b); and $R(\lambda)$ is the spectral internal reflectance of intensity in aperture area.

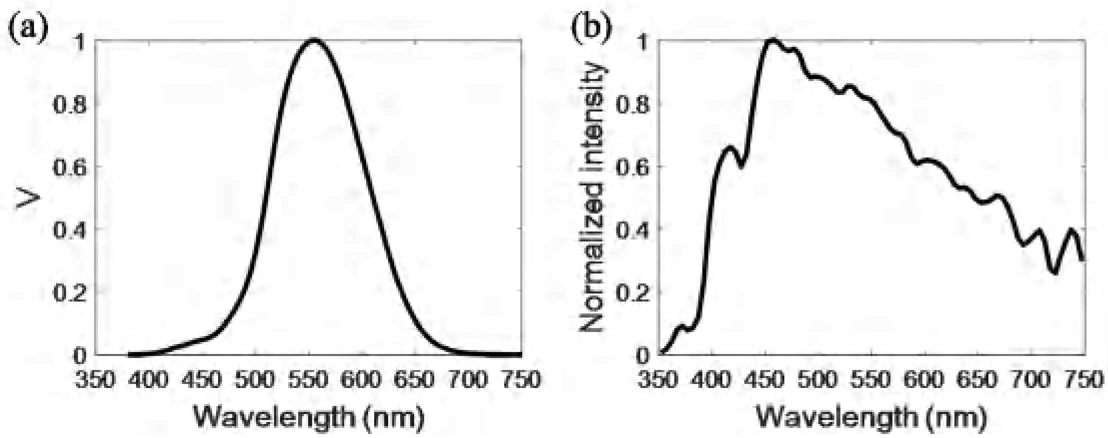

Figure 7-3 (a) Photopic human eye sensitivity function. (b) Spectrum of the ambient light (CIE Standard Illuminant D65).

R_{AP} is related to the optical structure. In CP-free RGB-chip mLED/μLED emissive displays, R_{AP} is mainly determined by LED bottom electrode and LED material. For instance, the luminous reflectance of blue LED varies from 5.4% on ITO (indium tin oxide) transparent electrode to 92.3% on silver reflective electrode. In the following simulation, we use high-conductivity gold electrode. Figure 7-4 depicts the $R(\lambda)$ of red AlGaInN LED and green/blue GaN LED with gold bottom electrode, corresponding to R_{AP} = [0.33, 0.67, 0.67] for [R, G, B] chip and 55.8% on average. In color conversion mLED/μLED emissive displays, ambient light excites quantum dots. The insertion of color filter (CF) helps suppress ambient excitation, which enables a drop of R_{AP} from 58.6% to 7.7%. On the other hand, some configurations do not suffer from internal reflection. In mLED-LCDs, ambient light is absorbed by the crossed linear polarizers in LCD. In RGB-chip mLED/μLED/OLED emissive displays, a circular polarizer can effectively cut off internal reflection. In these absorptive-polarizer-integrated systems, we take the approximation of $R_L \approx R_s$ because R_{AP} is negligible compared with R_s.

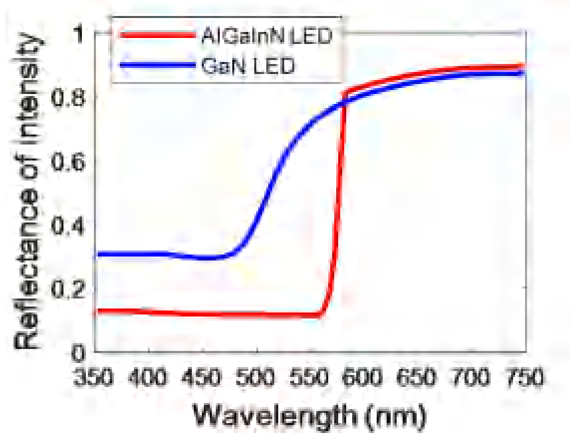

Figure 7-4 Spectral internal reflectance of red AlGaInN LED and green/blue GaN LED with gold bottom electrode.

Figure 7-5 depicts the simulated aperture ratio dependent ambient luminous reflectance of the specified display configurations. As expected, in CF-free color conversion (CC) mLED/μLED emissive displays (as shown by the blue line in Figure 7-5) and CP-free RGB-chip mLED/μLED emissive displays (as shown by the red line in Figure 7-5), R_L substantially increases as AP increases due to the high R_{AP}. The R_L of color conversion mLED/μLED emissive displays can be considerately lowered by an absorptive CF (as shown by the yellow line in Figure 7-5). Moreover, a lower R_L can be acquired in mLED-LCDs or CP-laminated RGB-chip mLED/μLED/OLED emissive displays (as shown by the purple line in Figure 7-5), where R_L is mainly determined by surface reflection rather than aperture ratio.

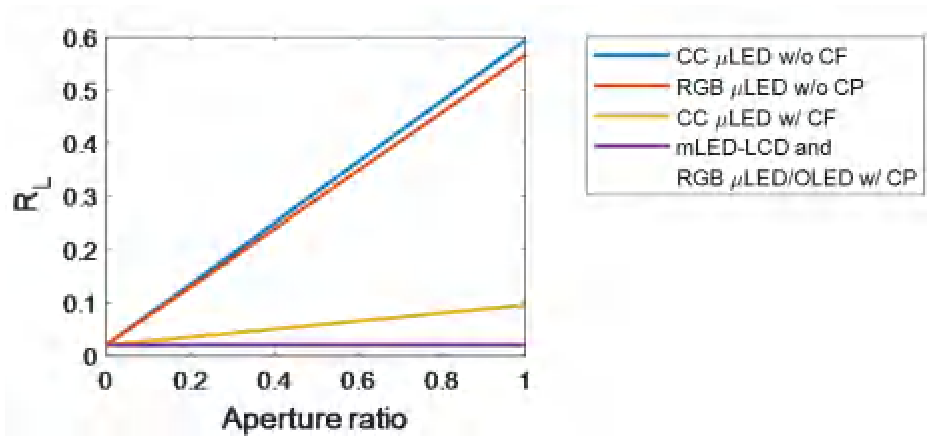

Figure 7-5 Aperture ratio dependent ambient luminous reflectance (R_L) of the specified display configurations.

7.3 Optimization strategy

In Chapter 6, we studied the size effect of mLED/μLED chips. As chip size becomes larger, EQE_{chip} increases [Figure 6-1(b)] and contributes to a desirable higher power efficiency [Figure 6-8]. Whereas, larger chip size also leads to larger AP and higher R_L (Figure 7-5), which makes ACR compromised [Equation (7-1)]. It is important to find a balance between panel power efficiency and panel luminance reflectance. Based on Equation (7-1), a reasonable assumption ACR >> 1, and Equation (6-11), we find

$$\begin{aligned} ACR &\approx \frac{\pi \cdot L_{on}}{I_{am} \cdot R_L} \\ &= \frac{\pi}{I_{am} \cdot R_L} \cdot \frac{P_{LED,W} \cdot \eta_W}{p^2} \\ &= \frac{\pi}{I_{am}} \cdot \frac{P_{panel}}{A_{panel}} \cdot \frac{\eta_W}{R_L}. \end{aligned} \quad \textbf{(7-4)}$$

In Equation (7-4), the first term π / I_{am} reflects the ambient environment; the second term P_{panel} / A_{panel} is specified by application; and the third term η_W / R_L originates from display optics. Because only the third term has the freedom of optimization, we define it as the figure-of-merit (FoM):

$$FoM = \frac{\eta_W}{R_L}. \tag{7-5}$$

Figure 7-6 delineates chip size dependent η_W / R_L for a 50-μm pitch smartphone [Figure 7-6(a)], a 156-μm pitch (27-inch 4K-resolution) gaming monitor [Figure 7-6(b)] and a 375-μm pitch (65-inch 4K-resolution) TV [Figure 7-6(c)]. In Figure 7-6, the black dashed lines denote a CP-laminated RGB-chip OLED emissive display, which has close-to-constant η_W and R_L so that η_W / R_L remains flat. The purple dashed lines stand for a mLED-LCD. Because large chips can be used in backlight unit, here we use R/G/B mLEDs with s = 100 μm in simulation. The red solid lines present CP-laminated RGB-chip mLED/μLED emissive displays, in which configuration large chip size boosts η_W and η_W / R_L. The blue solid lines and the yellow solid lines depict CP-free RGB-chip mLED/μLED emissive displays and CF-laminated color conversion mLED/μLED emissive displays, respectively. In these two CP-free structures, the small-chip side is impaired by Shockley-Read-Hall non-radiative recombination which results in low η_W; the large-chip side suffers from high AP indicating high R_L; the η_W / R_L peaks indicates the optimal choices.

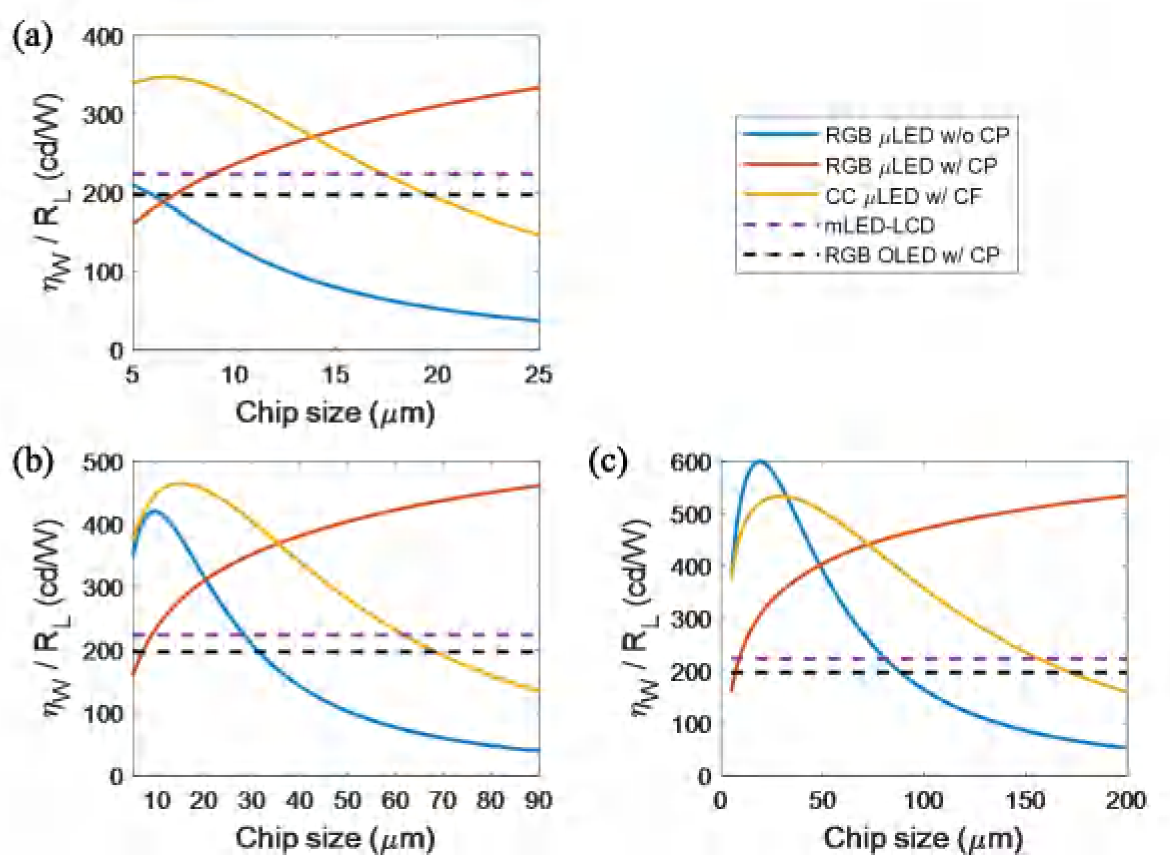

Figure 7-6 Chip size dependent η_W / R_L with different display technologies: (a) a 50-μm pitch smartphone, (b) a 156-μm pitch (27-inch 4K-resolution) gaming monitor, and (c) a 375-μm pitch (65-inch 4K-resolution) TV.

We can use Figure 7-6 to find the optimal system configuration and LED chip size by locating the highest η_W / R_L. Several messages are delivered in Figure 7-6: 1) As pixel pitch increases (from p = 50 μm in Figure 7-6(a) to p = 375 μm in Figure 7-6(c)), the maximum η_W / R_L becomes larger (from 347 cd/W in Figure 7-6(a) to 599 cd/W in Figure 7-6(c)). 2) At the large *AP* (large chip size) side, CP-laminated RGB-chip mLED/μLED emissive display wins. 3) At the small chip size side, CF-laminated color conversion type and CP-free RGB-chip μLED emissive display are the most competitive for panels with short pixel pitch (p < 220 μm) and long pixel pitch (p > 220 μm), respectively. With proper chip size and the same power supply, mLED/μLED displays can present 1.5 ~ 3× higher ACR than RGB-chip OLED emissive display and mLED-LCD.

Numerically, η_W / R_L can be used to estimate the ACR perceived by users. For example, Figure 7-6(c) is simulated for a 65-inch 4K-resolution TV (p = 375 μm, A_{panel} = 1.17 m^2). Using 19-μm μLEDs in CP-laminated RGB-chip structure, η_W / R_L can reach ~ 600 cd/W. Assuming P_{LED} = 95 W apart from the power consumption on panel electronics, the ACR in living room (I_{am} = 150 lux) exceeds 1000:1. Such a high ACR has not been achieved by state-of-the-art devices given the same panel specifications and viewing conditions. It is the potential of mLED/μLED displays.

7.4 Conclusion

In this chapter, we defined a figure-of-merit for systematically optimizing the ambient contrast ratio of mLED/μLED displays. Jointly considering power efficiency and ambient reflectance, we found the optimal system configuration and LED chip size according to applications: 1) CP-laminated RGB-chip type performs the best at large aperture ratio. 2) CF-laminated color conversion type and CP-free RGB-chip type are the most competitive with small LED chip size, while they respectively suit for panels with short pixel pitch (p < 220 μm) and long pixel pitch (p > 220 μm). Using our optimization strategy, mLED/μLED displays can achieve 1.5 ~ 3× higher ACR than state-of-the-art OLED displays and mLED-LCDs, and the power consumption is not compromised.

CHAPTER 8 CONCLUSION

In order to facilitate the development of the emerging mLED/μLED display technology, in this dissertation, we tackle with four key performance factors: response time, contrast ratio, power efficiency and ambient contrast ratio. Three system configurations – RGB-chip emissive display, color conversion emissive display and mini-LED backlit LCD – are specifically studied.

To suppress the motion blur of mLED-LCD, we advanced the status in two ways. From the aspect of image update delay, we proposed an image-corrected segmented progressive emission method, which breaks the tradeoff between image persistence time, data input time and duty ratio in conventional emission patterns. These three parameters determine motion blur, display resolution/panel size and peak luminance, respectively. Through subjective experiments, we verified our method's effectiveness, and recommend at least 180-Hz/preferred 360-Hz image content rate to diminish motion blur. Our new method achieves motion blur suppression on high-resolution, large-size and high-luminance panels.

From the aspect of LC response delay, we developed two types of submillisecond LC mixtures. The first mixture is a polymer-stabilized blue phase LC for flat panel displays. Our new mixture presents the outstanding features: 1) its fast response time helps mitigate motion blur. The slowest and average gray-to-gray response time are respectively < 2 ms and < 1 ms. 2) Its voltage holding ratio is adequate to support active operation. 3) Its blue phase temperature range (from −20°C to 75°C) is adequate for indoor applications. 4) Its average dielectric constant is 87, which is still below the upper limit for bootstrapping driving. Thus, it facilitates the signal capacity charging and reduces the data input time. 5) Using the triangular electrode structure, PSBP-08 can achieve 74% transmittance at 15 V, which enables single-TFT driving. 6) With two-domain structure, our blue phase LCD offers indistinguishable gamma shift and wide viewing angle.

The second effort resides in nematic LCs for LCoS-based augmented reality displays. Our new mixtures exhibit high birefringence to enable thin cell gap for fast response time, modest dielectric anisotropy for 5-V operation voltage, acceptable resistivity and UV stability, and wide nematic range. In experiment, these mixtures enable 2-ms response time in phase-only LCoS and submillisecond response time in MTN LCoS amplitude modulators. Our blue phase LC and nematic LCs will certainly alleviate motion blur defects.

For high contrast ratio (CR), we dealt with the biggest problem in local dimming mLED-LCD: halo effect and clipping effect. We developed a simplified model for simulating and optimizing mLED-LCD system. Through numerical simulation and subjective experiments, we find that halo effect and clipping effect be suppressed to an unnoticeable level by increasing LC CR and local dimming zone number. Specifically, we found that for a 6.4-inch smartphone at 25-cm distance, around 3000 and 200 local dimming zones are required for an FFS LCD with CR = 2000:1 and an MVA LCD panel with CR = 5000:1, respectively. These results can be extended to large-size panels according to the viewing distance. Besides, confining light in each local dimming zone can reduce inter-zone crosstalk, which alleviates halo effect and clipping effect from the root. We found that it is beneficial to have flattop spatial light profile for each local dimming zone, which significantly improves display fidelity from the Gaussian distribution generated from thick diffuser, and that is less vulnerable to backlight uniformity and misalignment tolerance issues than square-shaped profile.

For low power consumption, we built a new model for simulating and optimizing the power efficiency of mLED/μLED displays. we consider the size effect of inorganic mLED/μLED chips and applied the model to different system configurations. Our simulation results show that mLED-LCD is comparable power consuming as circular-polarizer-laminated RGB-chip OLED emissive display, while color-filter-laminated color conversion mLED/μLED emissive display, circular-polarizer-free and circular-polarizer-laminated RGB-chip mLED/μLED emissive displays respectively show up to 2.5×, up to 5× and up to 2× higher on-axis luminous power efficacy depending on the chip size of mLED/μLED. Moreover, based on inorganic LED characteristics, we demonstrated that small-aperture design and pulse width modulation are critical methods to achieve > 2× power saving.

For high ambient contrast ratio, we defined a figure-of-merit for systematically optimizing the structure of mLED/μLED displays. Jointly considering power efficiency and ambient reflectance, we found the optimal system configuration and LED chip size according to applications: 1) circular-polarizer-laminated RGB-chip type performs the best at large aperture ratio. 2) Color-filter-laminated color conversion type and circular-polarizer-free RGB-chip type are the most competitive with small chip size, while they respectively suit for panels with short pixel pitch (p < 220 μm) and long pixel pitch (p > 220 μm). Using our optimization strategy, mLED/μLED displays can achieve 1.5 ~ 3× higher ACR than state-of-the-art OLED displays and mLED-LCDs, and the power consumption is not compromised.

With our effects, attractive performance factors such as fast response time, high contrast ratio, low power consumption and high ambient contrast ratio can equip mLED/μLED displays. The shining of high fidelity mLED/μLED displays in the market is foreseeable.

APPENDIX: STUDENT PUBLICATIONS

JOURNAL PUBLICATIONS

1. (Invited) Huang, Y. *et al.* Prospects and challenges of mini-LED and micro-LED displays. *J. Soc. Inf. Disp.* **27**, 387–401 (2019).
2. (Review) Huang, Y., Liao, E., Chen, R. & Wu, S.-T. Liquid-crystal-on-silicon for augmented reality displays. *Appl. Sci.* **8**, 2366 (2018).
3. (Co-first author) Tan, G., Huang, Y., Li, M.-C., Lee, S.-L. & Wu, S.-T. High dynamic range liquid crystal displays with a mini-LED backlight. *Opt. Express* **26**, 16572–16584 (2018).
4. (OSA News) Huang, Y. *et al.* Optimized blue-phase liquid crystal for field-sequential-color displays. *Opt. Mater. Express* **7**, 641–650 (2017).
5. Huang, Y., He, Z. & Wu, S.-T. Fast-response liquid crystal phase modulators for augmented reality displays. *Opt. Express* **25**, 32757–32766 (2017).
6. Chen, R. *et al.* High-frame-rate liquid crystal phase modulator for augmented reality displays. *Liq. Cryst.* **46**, 309–315 (2019).
7. Talukder, J. R., Huang, Y. & Wu, S.-T. High performance LCD for augmented reality and virtual reality displays. *Liq. Cryst.* **46**, 920–929 (2019).
8. (OSA News) Peng, F. *et al.* High performance liquid crystals for vehicle displays. *Opt. Mater. Express* **6**, 717–726 (2016).
9. (Feature paper/AIP News) Liu, G. G. *et al.* Dielectric broadband meta-vector-polarizers based on nematic liquid crystal. *APL Photonics* **2**, 126102 (2017).

10. Chen, H. *et al.* A low voltage liquid crystal phase grating with switchable diffraction angles. *Sci. Rep.* **7**, 39923 (2017).

11. Peng, F., Gou, F., Chen, H., Huang, Y. & Wu, S.-T. A submillisecond-response liquid crystal for color sequential projection displays. *J. Soc. Inf. Disp.* **24**, 241–245 (2016).

12. (Review) Chen, H.-M. P. *et al.* Pursuing high quality phase-only liquid crystal on silicon (LCoS) devices. *Appl. Sci.* **8**, 2323 (2018).

13. Tan, G. *et al.* Review on polymer-stabilized short-pitch cholesteric liquid crystal displays. *J. Phys. D. Appl. Phys.* **50**, 493001 (2017).

CONFERENCE PROCEEDINGS

1. Huang, Y., Tan, G., Li, M.-C., Lee, S.-L. & Wu, S.-T. Mini-LED enhanced LCD for high dynamic range displays. *SID Symp. Dig. Tech. Pap.* **50**, 569–572 (2019).
2. Talukder, J. R., Huang, Y., & Wu, S.-T. High transmittance and fast response FFS LCD for AR and VR displays. *SID Symp. Dig. Tech. Pap.* **50**, 929–932 (2019).
3. Yang, J. P. *et al.* Submillisecond-response 10-megapixel 4K2K LCoS for microdisplay and spatial light modulator. *SID Symp. Dig. Tech. Pap.* **50**, 933–936 (2019).
4. Huang, Y., Tan, G., Li, M.-C., Lee, S.-L. & Wu, S.-T. Emerging high-dynamic-range mini-LED displays. *Proc. SPIE* **10942**, 1094205 (2019).
5. Huang, Y., Tan, G. & Wu, S.-T. Mini-LED enhanced high dynamic range LCD for automotive displays. *SID Veh. Displays Detroit Symp. Dig. Tech. Pap.* 4.7 (2018).
6. Huang, Y., He, Z. & Wu, S.-T. New liquid crystals enabling high-frame-rate LCoS for augmented reality displays. *SID Symp. Dig. Tech. Pap.* **49**, 589–592 (2018).
7. Chen, R. *et al.* High-birefringence liquid crystal for phase-only spatial light modulators. *SID Symp. Dig. Tech. Pap.* **49**, 674–677 (2018).
8. Chen, H. *et al.* New nematic LCD with submillisecond response time. *SID Symp. Dig. Tech. Pap.* **49**, 1691–1694 (2018).
9. Yang, J. P. *et al.* Sub-kHz 4000-ppi LCoS phase modulator for holographic displays. *SID Symp. Dig. Tech. Pap.* **49**, 772–775 (2018).
10. Huang, Y. *et al.* New blue-phase liquid crystal optimized for color-sequential displays. *SID Symp. Dig. Tech. Pap.* **48**, 486–489 (2017).

11. Peng, F. *et al.* High performance liquid crystals for vehicular displays. *SID Symp. Dig. Tech. Pap.* **47**, 754–756 (2016).

12. Peng, F. *et al.* A submillisecond-response liquid crystal for color-sequential projection displays. *SID Symp. Dig. Tech. Pap.* **47**, 179–182 (2016).

REFERENCES

1. Heilmeier, G. H., Zanoni, L. A. & Barton, L. A. Dynamic scattering: A new electrooptic effect in certain classes of nematic liquid crystals. *Proc. IEEE* **56**, 1162–1171 (1968).
2. Schadt, M. & Helfrich, W. Voltage-dependent optical activity of a twisted nematic liquid crystal. *Appl. Phys. Lett.* **18**, 127–128 (1971).
3. Schiekel, M. F. & Fahrenschon, K. Deformation of nematic liquid crystals with vertical orientation in electrical fields. *Appl. Phys. Lett.* **19**, 391–393 (1971).
4. Soref, R. A. Transverse field effects in nematic liquid crystals. *Appl. Phys. Lett.* **22**, 165–166 (1973).
5. Schadt, M. Milestone in the history of field-effect liquid crystal displays and materials. *Jpn. J. Appl. Phys.* **48**, 03B001 (2009).
6. Yang, D.-K. & Wu, S.-T. Fundamentals of liquid crystal devices (John Wiley & Sons, 2015).
7. Tang, C. W. & VanSlyke, S. A. Organic electroluminescent diodes. *Appl. Phys. Lett.* **51**, 913–915 (1987).
8. Baldo, M. A. *et al.* Highly efficient phosphorescent emission from organic electroluminescent devices. *Nature* **395**, 151–154 (1998).
9. Adachi, C., Baldo, M. A., Thompson, M. E. & Forrest, S. R. Nearly 100% internal phosphorescence efficiency in an organic light emitting device. *J. Appl. Phys.* **90**, 5048–5051 (2001).
10. Uoyama, H., Goushi, K., Shizu, K., Nomura, H. & Adachi, C. Highly efficient organic light-emitting diodes from delayed fluorescence. *Nature* **492**, 234–238 (2012).

11. Lee, J. H. *et al.* Blue organic light-emitting diodes: current status, challenges, and future outlook. *J. Mater. Chem. C* **7**, 5874–5888 (2019).

12. Buckley, A. Organic light-emitting diodes (OLEDs): materials, devices and applications (Woodhead Publishing Limited, 2013).

13. Tsujimura, T. OLED display fundamentals and applications (John Wiley & Sons, 2017).

14. Féry, C., Racine, B., Vaufrey, D., Doyeux, H. & Cinà, S. Physical mechanism responsible for the stretched exponential decay behavior of aging organic light-emitting diodes. *Appl. Phys. Lett.* **87**, 213502 (2005).

15. Murawski, C., Leo, K. & Gather, M. C. Efficiency roll-off in organic light-emitting diodes. *Adv. Mater.* **25**, 6801–6827 (2013).

16. Fan, R., Zhang, X. & Tu, Z. Influence of ambient temperature on OLED lifetime and uniformity based on modified equivalent lifetime detection. *J. Soc. Inf. Disp.* **27**, 597–607 (2019).

17. Jiang, H. X., Jin, S. X., Li, J., Shakya, J. & Lin, J. Y. III-nitride blue microdisplays. *Appl. Phys. Lett.* **78**, 1303–1305 (2001).

18. Jiang, H. X. & Lin, J. Y. Nitride micro-LEDs and beyond - a decade progress review. *Opt. Express* **21**, A475–A484 (2013).

19. Huang, Y. *et al.* Prospects and challenges of mini-LED and micro-LED displays. *J. Soc. Inf. Disp.* **27**, 387–401 (2019).

20. Wong, M. S., Nakamura, S. & DenBaars, S. P. Review—progress in high performance III-nitride micro-light-emitting diodes. *ECS J. Solid State Sci. Technol.* **9**, 015012 (2020).

21. Tan, G., Huang, Y., Li, M.-C., Lee, S.-L. & Wu, S.-T. High dynamic range liquid crystal displays with a mini-LED backlight. *Opt. Express* **26**, 16572–16584 (2018).

22. Kurita, T. Moving picture quality improvement for hold-type AM-LCDs. SID Symp. Dig. Tech. Pap. **32**, 986–989 (2001).

23. Peng, F. et al. Analytical equation for the motion picture response time of display devices. J. Appl. Phys. **121**, 023108 (2017).

24. Daly, S., Kunkel, T., Sun, X., Farrell, S. & Crum, P. Viewer preferences for shadow, diffuse, specular, and emissive luminance limits of high dynamic range displays. *SID Symp. Dig. Tech. Pap.* **44**, 563–566 (2013).

25. ST 2084:2014 High dynamic range electro-optical transfer function of mastering reference displays. (SMPTE, 2014).

26. Helman, J. L. Delivering high dynamic range video to consumer devices. *SID Symp. Dig. Tech. Pap.* **46**, 292–295 (2015).

27. Seetzen, H. *et al.* High dynamic range display systems. *ACM Trans. Graph.* **23**, 760–768 (2004).

28. Kim, S.-E. *et al.* How to reduce light leakage and clipping in local-dimming liquid-crystal displays. *J. Soc. Inf. Disp.* **17**, 1051–1057 (2009).

29. Chen, H., Ha, T. H., Sung, J. H., Kim, H. R. & Han, B. H. Evaluation of LCD local-dimming-backlight system. *J. Soc. Inf. Disp.* **18**, 57–65 (2010).

30. Hoffman, D. M., Stepien, N. N. & Xiong, W. The importance of native panel contrast and local dimming density on perceived image quality of high dynamic range displays. *J. Soc. Inf. Disp.* **24**, 216–228 (2016).

31. Olivier, F., Daami, A., Licitra, C. & Templier, F. Shockley-Read-Hall and Auger non-radiative recombination in GaN based LEDs: A size effect study. *Appl. Phys. Lett.* **111**, 022104 (2017).

32. Daami, A., Olivier, F., Dupré, L., Henry, F. & Templier, F. Electro-optical size-dependence investigation in GaN micro-LED devices. *SID Symp. Dig. Tech. Pap.* **49**, 790–793 (2018).

33. Chen, H., Tan, G. & Wu, S.-T. Ambient contrast ratio of LCDs and OLED displays. *Opt. Express* **25**, 33643–33656 (2017).

34. Li, C.-H. *et al.* Ultra-fast moving-picture response-time LCD for virtual reality application. *SID Symp. Dig. Tech. Pap.* **49**, 678–680 (2018).

35. Sluyterman, A. A. S. What is needed in LCD panels for achieving CRT-like motion portrayal? *J. Soc. Inf. Disp.* **14**, 681–686 (2006).

36. Kikuchi, H., Yokota, M., Hisakado, Y., Yang, H. & Kajiyama, T. Polymer-stabilized liquid crystal blue phases. *Nat. Mater.* **1**, 64–68 (2002).

37. Yan, J. *et al.* Polymer-stabilized optically isotropic liquid crystals for next-generation display and photonics applications. *J. Mater. Chem. C Mater. Opt. Electron. Devices* **21**, 7870-7877 (2011).

38. Huang, Y. *et al.* Optimized blue-phase liquid crystal for field-sequential-color displays. *Opt. Mater. Express* **7**, 641–650 (2017).

39. Ge, Z., Rao, L., Gauza, S. & Wu, S. Modeling of blue phase liquid crystal displays. *J. Disp. Technol.* **5**, 250–256 (2009).

40. Lee, H. *et al.* The world's first blue phase liquid crystal display. *SID Symp. Dig. Tech. Pap.* **42**, 121–124 (2011).

41. Tsai, C. Y. *et al.* A novel blue phase liquid crystal display applying wall-electrode and high driving voltage circuit. *SID Symp. Dig. Tech. Pap.* **46**, 542–544 (2015).

42. Rao, L., Ge, Z., Wu, S. T. & Lee, S. H. Low voltage blue-phase liquid crystal displays. *Appl. Phys. Lett.* **95**, 231101 (2009).

43. Kim, M. *et al.* Wall-shaped electrodes for reducing the operation voltage of polymer-stabilized blue phase liquid crystal displays. *J. Phys. D: Appl. Phys.* **42**, 235502 (2009).

44. Rao, L., Yan, J., Wu, S. T., Yamamoto, S. I. & Haseba, Y. A large Kerr constant polymer-stabilized blue phase liquid crystal. *Appl. Phys. Lett.* **98**, 081109 (2011).

45. Chen, Y., Xu, D., Wu, S. T., Yamamoto, S. I. & Haseba, Y. A low voltage and submillisecond-response polymer-stabilized blue phase liquid crystal. *Appl. Phys. Lett.* **102**, 141116 (2013).

46. Peng, F. *et al.* Low temperature and high frequency effects on polymer-stabilized blue phase liquid crystals with large dielectric anisotropy. *J. Mater. Chem. C Mater. Opt. Electron. Devices* **2**, 3597-3601 (2014).

47. Wittek, M. *et al.* New materials for polymer-stabilized blue phase. *SID Symp. Dig. Tech. Pap.* **43**, 25–28 (2012).

48. Haseba, Y., Yamamoto, S. I., Sago, K., Takata, A. & Tobata, H. Low-voltage polymer-stabilized blue-phase liquid crystals. *SID Symp. Dig. Tech. Pap.* **44**, 254–257 (2013).

49. Tu, C. D. *et al.* Driving scheme using bootstrapping method for blue-phase LCDs. *J. Disp. Technol.* **9**, 3–6 (2013).

50. Lin, C. L. *et al.* Novel dual-coupling pixel circuit to achieve high transmittance of blue-phase liquid crystal. *IEEE Electron Device Lett.* **36**, 354–356 (2015).

51. Li, Y. *et al.* Dielectric dispersion on the Kerr constant of blue phase liquid crystals. *Appl. Phys. Lett.* **99**, 181126 (2011).

52. Chen, Y. & Wu, S. T. Recent advances on polymer-stabilized blue phase liquid crystal materials and devices. *J. Appl. Polym. Sci.* **131**, 40556 (2014).

53. Wu, P. C., Hsu, H. T., Chen, H. L. & Lee, W. Dielectric characterization and voltage holding ratio of blue-phase cells. *Displays* **44**, 66–72 (2016).

54. Yan, J. *et al.* Extended Kerr effect of polymer-stabilized blue-phase liquid crystals. *Appl. Phys. Lett.* **96**, 071105 (2010).

55. Gerber, P. R. Electro-Optical Effects of a Small-Pitch Blue-Phase System. *Mol. Cryst. Liq. Cryst.* **116**, 197–206 (1985).

56. Wu, S.-T. Birefringence dispersions of liquid crystals. *Phys. Rev. A Gen. Phys.* **33**, 1270–1274 (1986).

57. Hird, M. Fluorinated liquid crystals – properties and applications. *Chem. Soc. Rev.* **36**, 2070–2095 (2007).

58. Ishitani, T. *et al.* High-performance polymer-stabilized blue-phase LCD with low driving voltage. *J. Soc. Inf. Disp.* **21**, 9–15 (2013).

59. Yoon, S. *et al.* Optimisation of electrode structure to improve the electro-optic characteristics of liquid crystal display based on the Kerr effect. *Liq. Cryst.* **37**, 201–208 (2010).

60. Li, Y. *et al.* Transmissive and Transflective Blue-Phase LCDs with Double-Layer IPS Electrodes. *J. Disp. Technol.* **12**, 122–128 (2016).

61. Liu, J., Ma, H. & Sun, Y. Blue-phase liquid crystal display with high dielectric material. *Liq. Cryst.* **43**, 1748–1752 (2016).

62. Yamamoto, T. *et al.* Crystalline OS-LCD using blue-phase liquid crystal having characteristic texture. *SID Symp. Dig. Tech. Pap.* **43**, 201–204 (2012).

63. Kubota, D., Yamashita, A. & Nakano, M. Liquid crystal display device. (2014).

64. Rao, L., Ge, Z. & Wu, S. T. Zigzag electrodes for suppressing the color shift of Kerr effect-based liquid crystal displays. *J. Disp. Technol.* **6**, 115–120 (2010).

65. Kim, S. S., Berkeley, B. H., Kim, K. H. & Song, J. K. New technologies for advanced LCD-TV performance. *J. Soc. Inf. Disp.* **12**, 353–359 (2004).

66. Gao, Y. *et al.* A high performance single-domain LCD with wide luminance distribution. *J. Disp. Technol.* **11**, 315–324 (2015).

67. Huang, Y., He, Z. & Wu, S.-T. Fast-response liquid crystal phase modulators for augmented reality displays. *Opt. Express* **25**, 32757–32766 (2017).

68. Armitage, D., Underwood, I. & Wu, S.-T. Introduction to microdisplays (John Wiley & Sons, 2006).

69. Handschy, M. A., McNeil, J. R. & Weissman, P. E. Ultrabright head-mounted displays using LED-illuminated LCOS. *Proc. SPIE* **6224**, 62240S (2006).

70. Chen, H.-M. P. *et al.* Pursuing high quality phase-only liquid crystal on silicon (LCoS) devices. *Appl. Sci.* **8**, 2323 (2018).

71. Huang, Y., Liao, E., Chen, R. & Wu, S.-T. Liquid-crystal-on-silicon for augmented reality displays. *Appl. Sci.* **8**, 2366 (2018).

72. Maimone, A., Georgiou, A. & Kollin, J. S. Holographic near-eye displays for virtual and augmented reality. *ACM Trans. Graph.* **36**, 85 (2017).

73. Matsuda, N., Fix, A. & Lanman, D. Focal surface displays. *ACM Trans. Graph.* **36**, 86 (2017).

74. Wu, S.-T. & Wu, C.-S. Mixed-mode twisted nematic liquid crystal cells for reflective displays. *Appl. Phys. Lett.* **68**, 1455–1457 (1996).

75. Kuo, C.-L., Wei, C.-K., Wu, S.-T. & Wy, C.-S. Reflective direct-view display using a mixed-mode twisted nematic cell. *Jpn. J. Appl. Phys.* **36**, 1077–1080 (1997).

76. Alt, P. M. Single crystal silicon for high resolution displays. *Proc. 17th Int. Disp. Res. Conf.* M19–M28 (1997).

77. Sun, J. & Wu, S.-T. Recent advances in polymer network liquid crystal spatial light modulators. *J. Polym. Sci. Part B Polym. Phys.* **52**, 183–192 (2014).

78. Tan, G. *et al.* Review on polymer-stabilized short-pitch cholesteric liquid crystal displays. *J. Phys. D. Appl. Phys.* **50**, 493001 (2017).

79. Srivastava, A. K., Chigrinov, V. G. & Kwok, H. S. Ferroelectric liquid crystals: Excellent tool for modern displays and photonics. *J. Soc. Inf. Disp.* **23**, 253–272 (2015).

80. Chen, Y. *et al.* High birefringence fluoro-terphenyls for thin-cell-gap TFT-LCDs. *J. Disp. Technol.* **7**, 478–481 (2011).

81. Gauza, S. *et al.* High birefringence isothiocyanato tolane liquid crystals. *Jpn. J. Appl. Phys.* **42**, 3463–3466 (2003).

82. Dąbrowski, R., Kula, P. & Herman, J. High birefringence liquid crystals. *Crystals* **3**, 443–482 (2013).

83. Chen, H., Peng, F., Hu, M. & Wu, S. T. Flexoelectric effect and human eye perception on the image flickering of a liquid crystal display. *Liq. Cryst.* **42**, 1730–1737 (2015).

84. Wu, S.-T., Efron, U. & Hess, L. D. Birefringence measurements of liquid crystals. *Appl. Opt.* **23**, 3911–3915 (1984).

85. Haller, I. Thermodynamic and static properties of liquid crystals. *Prog. Solid State Chem.* **10**, 103–118 (1975).

86. Beeson, K. *et al.* LED-based light-recycling light sources for projection displays. *SID Symp. Dig. Tech. Pap.* **37**, 1823–1826 (2006).

87. Wu, S.-T. & Wu, C.-S. Rotational viscosity of nematic liquid crystals A critical examination of existing models. *Liq. Cryst.* **8**, 171–182 (1990).

88. Wen, C.-H., Gauza, S. & Wu, S.-T. Photostability of liquid crystals and alignment layers. *J. Soc. Inf. Disp.* **13**, 805–811 (2005).

89. Sun, J., Chen, Y. & Wu, S.-T. Submillisecond-response and scattering-free infrared liquid crystal phase modulators. *Opt. Express* **20**, 20124–20129 (2012).

90. Hasebe, H. & Kobayashi, S. A full-color field sequential LCD using modulated backlight. *SID Symp. Dig. Tech. Pap.* **16**, 81–83 (1985).

91. Huang, Y. P., Lin, F. C. & Shieh, H. P. D. Eco-displays: the color LCD's without color filters and polarizers. *J. Disp. Technol.* **7**, 630–632 (2011).

92. Wu, S.-T. Design of a liquid crystal based tunable electrooptic filter. *Appl. Opt.* **28**, 48–52 (1989).

93. Deng, Z. *et al.* High dynamic range incell LCD with excellent performance. *SID Symp. Dig. Tech. Pap.* **49**, 996–998 (2018).

94. Hulze, H. G., deGreef, P. Power savings by local dimming on a LCD panel with side lit backlight. *SID Symp. Dig. Tech. Pap.* **40**, 749–752 (2009).

95. Chen, H., Ha, T. H., Sung, J. H., Kim, H. R. & Han, B. H. Evaluation of LCD local-dimming-backlight system. *J. Soc. Inf. Disp.* **18**, 57–65 (2010).

96. Burini, N., Nadernejad, E., Korhonen, J., Forchhammer, S. & Wu, X. Modeling power-constrained optimal backlight dimming for color displays. *J. Disp. Technol.* **9**, 656–665 (2013).

97. Zwillinger D. & Kokoska S. CRC standard probability and statistics tables and formulae (Chapman & Hall/CRC, 2000).

98. Sun, C. *et al.* Calculating model of light transmission efficiency of diffusers attached to a lighting cavity. *Opt. Express* **18**, 6137–6148 (2010).

99. Woodgate, G. J. *et al.* Micro-optical systems for micro-LED displays. *SID Symp. Dig. Tech. Pap.* **49**, 1559–1562 (2018).

100. Gou, F. *et al.* Angular color shift of micro-LED displays. *Opt. Express* **27**, A746–A757 (2019).

101. Ahmed, K. Micro LEDs efficiency targets for displays. *SID Symp. Dig. Tech. Pap.* **50**, 125–128 (2019).

102. Jung, T., Choi, J. H., Jang, S. H. & Han, S. J. Review of micro-light-emitting-diode technology for micro-display applications. *SID Symp. Dig. Tech. Pap.* **50**, 442–446 (2019).

103. Lee, E. *et al.* Quantum dot conversion layers through inkjet printing. *SID Symp. Dig. Tech. Pap.* **49**, 525–527 (2018).

104. Chen, G.-S., Wei, B.-Y., Lee, C.-T. & Lee, H.-Y. Monolithic red/green/blue micro-LEDs with HBR and DBR structures. *IEEE Photonics Technol. Lett.* **30**, 262–265 (2018).

105. Kim, H.-J., Shin, M.-H., Kim, J.-S. & Kim, Y.-J. Optical efficiency enhancement in wide color gamut LCD by a patterned quantum dot film and short pass reflector. *SID Symp. Dig. Tech. Pap.* **47**, 827–829 (2016).

106. Kim, K. H. *et al.* Phosphorescent dye-based supramolecules for high-efficiency organic light-emitting diodes. *Nat. Commun.* **5**, 4769 (2014).

107. Hosoumi, S. *et al.* Ultra-wide color gamut OLED display using a deep-red phosphorescent device with high efficiency, long life, thermal stability, and absolute BT.2020 red chromaticity. *SID Symp. Dig. Tech. Pap.* **48**, 13–16 (2017).

108. Sasabe, H. *et al.* Extremely low operating voltage green phosphorescent organic light-emitting devices. *Adv. Funct. Mater.* **23**, 5550–5555 (2013).

109. Takita, Y. *et al.* Highly efficient deep-blue fluorescent dopant for achieving low-power OLED display satisfying BT.2020 chromaticity. *J. Soc. Inf. Disp.* **26**, 55–63 (2018).